

Spectroscopic Modeling of Luminous Transients Powered by H-Rich and He-Rich Circumstellar Interaction

GURURAJ A. WAGLE ¹, EMMANOUIL CHATZOPOULOS ^{2,3} AND MICHAEL J. BAER ²

¹*Institut d'Astronomie et d'Astrophysique, CP-226, Université Libre de Bruxelles, B-1050, Brussels, Belgium*

²*Department of Physics and Astronomy, Louisiana State University, Baton Rouge, LA 70803, USA*

³*Institute of Astrophysics, Foundation for Research and Technology-Hellas (FORTH), Heraklion, 70013, Greece*

(Received 21 July, 2024; Revised 11 November, 2024; Accepted 16 November, 2024)

ABSTRACT

In this study, we perform detailed spectroscopic modeling to analyze the interaction of circumstellar material (CSM) with ejecta in both hydrogen-rich and hydrogen-poor superluminous supernovae (SLSNe), systematically varying properties such as CSM density, composition, and geometry to explore their effects on spectral lines and light curve evolution. Using advanced radiative transfer simulations with the new, open-source SuperLite code to generate synthetic spectra, we identify key spectroscopic indicators of CSM characteristics. Our findings demonstrate that spectral lines of hydrogen and helium exhibit significant variations due to differences in CSM mass and composition. In hydrogen-rich SLSN-II, we observe pronounced hydrogen emission lines that correlate strongly with dense, extended CSM, suggesting massive, eruptive mass-loss histories. Conversely, in hydrogen-poor SLSNe, we recover mostly featureless spectra at early times, with weak hydrogen lines appearing only in the very early phases of the explosion, highlighting the quick ionization of traces of hydrogen present in the CSM. We analyze the properties of the resulting emission lines, particularly H_α and H_β, for our models using sophisticated statistical methods. This analysis reveals how variations in the supernova progenitor and CSM properties can lead to distinct spectroscopic evolutions over time. These temporal changes provide crucial insights into the underlying physics driving the explosion and the subsequent interaction with the CSM. By linking these spectroscopic observations to the initial properties of the progenitor and its surrounding material, our study offers a useful tool for probing the pre-explosion history of these explosive events.

Keywords: Radiative transfer (1335), Monte Carlo methods (2238), Supernovae (1668), Circumstellar shells (242), Transient sources (1851), Stellar-interstellar interactions (1576)

1. INTRODUCTION

Over the last twenty years, the time-domain astrophysics community has been captivated by the discovery of extremely luminous and exotic transient phenomena, sparking rigorous theoretical studies aiming to explain their origins. The high-cadence, wider field-of-view surveys conducted by Pan-STARRS (Panoramic Survey Telescope and Rapid Response System Kaiser et al. 2002), the Large Synoptic Survey Telescope (LSST Ivezic et al. 2008), ASAS-SN (All-Sky Automated Sur-

vey for Supernovae Shappee et al. 2014), and ZTF (Zwicky Transient Facility Bellm et al. 2019) are continuously discovering new instances of rare, luminous events. Among these revelations, the super luminous supernovae (SLSNe) stand out as particularly enigmatic (Quimby et al. 2011; Gal-Yam 2012). The SLSNe, coined for their peak luminosities exceeding their classical counterparts by over 2 magnitudes, challenge our traditional understanding of the mechanisms that source the normal SNe, viz., SN shock waves and radioactive decay of ⁵⁶Ni. The high luminosity of the SLSNe make them detectable from large distances, and hence they are valuable for probing distant galaxies. SLSNe have been observed spectroscopically to redshifts up to $z \approx$

2 (Smith et al. 2018), and photometrically up to $z \approx 4$ (Cooke et al. 2012).

In spite of the increase in their discovery rate, the SLSNe are rare events. Only ~ 1 SLSN is observed in a volumetric sample per few thousand SNe (Quimby et al. 2013). This sparsity of sample has led to several unanswered questions regarding the observed diversity in the photometric and spectroscopic properties of the SLSNe and the underlying mechanisms that power these luminous events. The majority of the observed SLSNe are hydrogen-poor in their observed spectra, with strong O II absorption lines early on (Quimby et al. 2011; Inserra et al. 2013). These SLSNe are referred to as type-I (SLSN-I) analogous to traditional type I SNe (SN-I). About 150 SLSNe-I have been confirmed spectroscopically (Gomez et al. 2020). The other group of SLSN shows strong, narrow hydrogen emission lines in their spectra, analogous to traditional type IIIn SNe (SN-IIIn). Despite the smaller sample size, there are well-studied examples of SLSN-II such as SN 2006gy (Ofek et al. 2007; Smith et al. 2007), SN 2006tf (Smith et al. 2008), SN 2008fz (Drake et al. 2010), and SN 2008am (Chatzopoulos et al. 2011).

Among the competing theories to explain the immense amount of power required to explain the luminosities of SLSNe, two are more widely accepted given their success in explaining both the luminosities and the timescales of the observed light curves (Nicholl 2021). The first of these is a highly magnetized, rapidly rotating (millisecond) pulsar (magnetar Kasen & Bildsten 2010; Woosley 2010). Observed galactic neutron stars have periods larger than a millisecond, however, conservation of angular momentum points to a possibility that they might have been born with a much lower period (Duncan & Thompson 1992). The other competing theory points to an interaction between slow-moving circumstellar material (CSM) and SN ejecta (Chevalier & Fransson 1994; Smith & McCray 2007; Chatzopoulos et al. 2012; Chevalier & Irwin 2011; Ginzburg & Balberg 2012).

The narrow hydrogen emission lines observed in SLSNe-II indicate strong SN ejecta-circumstellar material interaction (hereafter, CSI), as observed in the classical SN-IIIn (Schlegel 1990). Spectroscopic models of interacting SNe have been studied mostly in the context of regular-luminosity, H-rich Type IIIn events involving collisions between red supergiant (RSG) progenitor SN ejecta and a dense H-rich wind (Dessart et al. 2015, 2016, 2022; Dessart & Jacobson-Galán 2023; Dessart et al. 2023, 2024). These spectroscopic models, which are mainly performed with the CMFGEN code (Dessart & Hillier 2010) have significantly aided the effort to elucidate the properties of the CSM and the progenitor

stars, but their application has been limited to regular-luminosity events and H-rich environments. Synthetic spectra for SLSNe interacting with H-deficient CSM of different structural properties (such as density profile and distance from the progenitor stars) are still necessary to further determine the prevalence of CSM interaction for SLSNe and other luminous transients that do not show signs of H in their spectra.

Even though it is difficult to clearly distinguish magnetar model from the CSI as the mechanism that powers the SLSNe (Metzger et al. 2014), Benetti et al. (2014) make an argument that the two spectroscopic classes with and without the hydrogen lines, SLSN-I and SLSN-II could be explained by the same underlying mechanism. In the context of CSS121015, a SLSN-Ic, they found that the observed properties are more consistent with a CSI model over a magnetar model. They further propose that the diversity in the observed properties of different subtypes of SLSNe could be explained in terms of the differences in the structure and hydrogen content of the CSM.

In this study, we explore the effects on the light curves and spectra of SLSNe for a range of progenitor models combined with a range of circumstellar properties. In section 2, we explain the numerical methods employed to evolve the progenitor stars and the SN ejecta. In section 3, we present the results of our simulations, namely, the evolution of the bolometric luminosity and the spectra for our models. We present a statistical analysis partially driven by supervised machine learning (ML) techniques performed on the data to find the correlation between the model parameters and the strength of the Balmer series lines. We also present a comparison of our model spectra with the observed SN spectra. Finally, we discuss the conclusions of our study.

2. NUMERICAL METHODS

We explored the evolution of the progenitors and the properties of their subsequent SN explosion through the following numerical setup. The evolution of the progenitors was carried out using stellar evolution code Modules for Experiments in Stellar Astrophysics (MESA, Paxton et al. 2011, 2013, 2015, 2018, 2019), followed by the radiation hydrodynamic code STELLA (Blinnikov & Bartunov 1993; Blinnikov et al. 1998; Blinnikov & Sorokina 2004; Blinnikov et al. 2006) to track the time evolution of the SN ejecta. In the final step, the spectroscopic properties were extracted using a Monte Carlo radiative

transfer code `SuperLite`¹ (Wagle et al. 2023) by mapping the hydrodynamic profiles of the resulting SN from `STELLA`. We discuss each of these steps in detail in the following sections.

2.1. Progenitor evolution

We calculated the evolution of three isolated massive progenitor stars using `MESA`. The progenitor stars were evolved with initial properties chosen to produce a red supergiant (RSG; with the supernova mass, $M_{\text{SN}} = 17.8 M_{\odot}$ and the radius $R_{\text{SN}} = 603 R_{\odot}$), a yellow supergiant (YSG; $M_{\text{SN}} = 11.6 M_{\odot}$, $R_{\text{SN}} = 525 R_{\odot}$) and a blue supergiant (BSG; $M_{\text{SN}} = 3.4 M_{\odot}$, $R_{\text{SN}} = 7.24 R_{\odot}$) as a pre-explosion model. This choice was made to investigate the effects of SN ejecta mass and composition, and the CSM composition, on the resulting spectral evolution for a variety of different initial conditions. For all the computed `MESA` models, we adopted solar metallicity (Asplund et al. 2009) at Zero Age Main Sequence, no rotation, a Ledoux criterion for convection with the mixing-length parameter $\alpha_{\text{MLT}}=1.5$, a 21-isotope nuclear reaction network, and the “Dutch” mass-loss prescription (Nugis & Lamers 2000; Vink et al. 2001; Glebbeek et al. 2009) that is recommended for massive stars within our target SN progenitor mass range².

For each of the three progenitors, we used the same method described in Paxton et al. (2018) to produce 1D, spherically symmetric SN explosions corresponding to three different SN explosion energy choices for each model (low, medium, and high SN explosion energy; see Table 1). The composition of the CSM is set to be the same as the surface composition of the progenitor star that resulted from the `MESA` simulation, as the CSM consists of the steady-state winds produced in the latest stages of the stellar evolution. In each case, we evolved the SN shock wave until the point before the shock break-out from the stellar surface. Subsequently, for the majority of the resulting pre-explosion models, we appended wind-like CSM structures following the r^{-2} density law corresponding to different mass-loss rates (\dot{M}_{CSM}) and wind velocities (v_{CSM}) which, in turn, translate to different mass-loss timescales (t_{CSM}) and total CSM masses (M_{CSM}). The CSM properties

listed in Table 1 for each model series were set to represent the typical properties based on the types of progenitors they represent. Model C progenitors are akin to WR-star progenitors with strong winds that have lost their H envelopes. For these compact stars, characteristic wind speeds are typically higher ($\sim 1,000$ km/s), and mass loss timescales are typically lower (M/\dot{M} decreases for an increasing \dot{M}). The mass-loss takes place at a later stage, therefore the total radius of the CSM created assuming steady-state winds is $\sim 10^{15}$ cm; shorter than that typical of RSGs and BSGs (which can extend to $\sim \times 10^{16}$ cm). This resulted in a total of 45 models of different initial progenitor and CSM conditions, with their properties detailed in Table 1. From hereafter, we will refer to the RSG progenitor models as “Series A”, the YSG progenitor models as “Series B” and the BSG progenitor models as “Series C”.

All 45 explosions were then processed with the two-temperature radiation transfer code `STELLA` (Blinnikov et al. 1998, 2006). `STELLA` solves the radiative transfer equations in the intensity momentum approximation in each frequency bin and computes bolometric and broad-band light curves of SN explosions, including for those affected by the interaction with a CSM. `STELLA` is offered within each `MESA` code release, allowing for a smooth transition between the two codes to facilitate the modeling of SN explosions. `STELLA` also yields radiation hydrodynamics profiles for several phases following the explosion, providing the inputs we need to compute time-series of synthetic spectra for each SN model processed.

2.2. Radiative transfer calculations with SuperLite

We use the hydrodynamic profiles generated by `STELLA` at several checkpoints through about 30-50 days since the beginning of the `STELLA` simulation for the three model series. The profiles are processed with the time-independent radiation transport code `SuperLite`. The profiles are truncated at a Rosseland mean optical depth of 100, as computed by `STELLA`. As noted in Wagle et al. (2023), an optical depth of 30-50 is sufficient for correctly predicting the transitions of lines in the region of interest. We choose a value of 100 to be exhaustive. We choose 6000 wavelength groups with a range of 1 to 30,000 Å for the radiative transfer calculations. The hydrodynamic profiles contain the kinetic and radiation temperature profiles, along with the other properties. About a million (2^{20}) MC particles are instantiated for the simulation using the radiation temperature provided in the hydrodynamic profile. The spectra are evaluated assuming local thermodynamic equilibrium (LTE) for the line opacities and emissivities. The ionization bal-

¹ Publicly available at Github (https://gururajw.github.io/superlite_docs/) and Zenodo (Wagle 2023) for download. The code documentation is provided at https://gururajw.github.io/superlite_docs/.

² The inlist files are available on Zenodo under an open-source Creative Commons Attribution license: [doi:10.5281/zenodo.13890925](https://doi.org/10.5281/zenodo.13890925).

Table 1. Properties of the Progenitors and the CSM.

		Model	Explosion Energy [10^{51} erg]	^{56}Ni mass [M_{\odot}]	M_{CSM} [M_{\odot}]	\dot{M}_{CSM} [M_{\odot}/yr]	v_{CSM} [kms^{-1}]	t_{CSM} [yr]	CSM composition
A Series - Red Super Giant	Radius at explosion 603 R_{\odot}	A1	0.78	0.042	0.0	N/A	N/A	N/A	N/A
		A2	1.0	0.042	0.0	N/A	N/A	N/A	N/A
		A3	1.2	0.042	0.0	N/A	N/A	N/A	N/A
		A4	0.78	0.042	0.2	0.025	200	8	H-rich
		A5	0.78	0.042	0.5	0.0625	200	8	H-rich
	Mass at explosion 17.8 M_{\odot}	A6	0.78	0.042	1.0	0.125	200	8	H-rich
		A7	0.78	0.042	1.2	0.25	200	8	H-rich
		A8	1.0	0.042	0.2	0.025	200	8	H-rich
		A9	1.0	0.042	0.5	0.0625	200	8	H-rich
		A10	1.0	0.042	1.0	0.125	200	8	H-rich
	Mass at ZAMS 19 M_{\odot}	A11	1.0	0.042	1.2	0.25	200	8	H-rich
		A12	1.2	0.042	0.2	0.025	200	8	H-rich
		A13	1.2	0.042	0.5	0.0625	200	8	H-rich
		A14	1.2	0.042	1.0	0.125	200	8	H-rich
		A15	1.2	0.042	1.2	0.25	200	8	H-rich
B Series - Yellow Super Giant	Radius at explosion 525 R_{\odot}	B1	0.28	0.009	0.0	N/A	N/A	N/A	N/A
		B2	0.5	0.009	0.0	N/A	N/A	N/A	N/A
		B3	1.0	0.009	0.0	N/A	N/A	N/A	N/A
		B4	0.28	0.009	0.2	0.025	200	8	H-rich
		B5	0.28	0.009	0.5	0.0625	200	8	H-rich
	Mass at explosion 11.6 M_{\odot}	B6	0.28	0.009	1.0	0.125	200	8	H-rich
		B7	0.28	0.009	1.2	0.25	200	8	H-rich
		B8	0.5	0.009	0.2	0.025	200	8	H-rich
		B9	0.5	0.009	0.5	0.0625	200	8	H-rich
		B10	0.5	0.009	1.0	0.125	200	8	H-rich
	Mass at ZAMS 11.8 M_{\odot}	B11	0.5	0.009	1.2	0.25	200	8	H-rich
		B12	1.0	0.009	0.2	0.025	200	8	H-rich
		B13	1.0	0.009	0.5	0.0625	200	8	H-rich
		B14	1.0	0.009	1.0	0.125	200	8	H-rich
		B15	1.0	0.009	1.2	0.25	200	8	H-rich
C Series - Blue Super Giant	Radius at explosion 7.24 R_{\odot}	C1	0.80	0.011	0.0	N/A	N/A	N/A	N/A
		C2	0.95	0.011	0.0	N/A	N/A	N/A	N/A
		C3	1.50	0.011	0.0	N/A	N/A	N/A	N/A
		C4	0.80	0.011	0.2	0.2	1000	1	He-rich
		C5	0.80	0.011	0.4	0.4	1000	1	He-rich
	Mass at explosion 3.4 M_{\odot}	C6	0.80	0.011	1.0	1.0	1000	1	He-rich
		C7	0.80	0.011	2.0	2.0	1000	1	He-rich
		C8	0.95	0.011	0.2	0.2	1000	1	He-rich
		C9	0.95	0.011	0.4	0.4	1000	1	He-rich
		C10	0.95	0.011	1.0	1.0	1000	1	He-rich
	Mass at ZAMS 11 M_{\odot}	C11	0.95	0.011	2.0	2.0	1000	1	He-rich
		C12	1.50	0.011	0.2	0.2	1000	1	He-rich
		C13	1.50	0.011	0.4	0.4	1000	1	He-rich
		C14	1.50	0.011	1.0	1.0	1000	1	He-rich
		C15	1.50	0.011	2.0	2.0	1000	1	He-rich

NOTE—The H-rich CSM composition contains $X(\text{H}) \approx 0.64$ and $X(\text{He}) \approx 0.34$, while the He-rich CSM composition contains $X(\text{H}) \approx 0$ and $X(\text{He}) \approx 0.84$. The composition of the CSM is set to be the same as the surface composition of the progenitor star based on the results of the corresponding MESA simulation.

ance is calculated using the Saha equation and the excitation level populations are calculated using Boltzmann statistics under the LTE assumption, using the electron temperature. We also calculate the spectra for non-LTE (NLTE) conditions by solving the rate equation matrix for hydrogen line transitions as described in [Wagle et al. \(2023\)](#).

3. RESULTS

In this section, we present the results of our hydrodynamic and radiative transfer simulations for the three series of models: A, B, and C. The following subsections discuss the photometric and spectroscopic evolution of these models and the significance of the CSM interaction. We then analyze the fluxes of the dominant H Balmer series lines H_α and H_β , and their ratio, $F(H_\alpha)/F(H_\beta)$. In the final subsection, we compare the spectral synthesis results of the `SuperLite` code to the observed spectra.

3.1. Light curve evolution

In Figures 1 to 3, we present the bolometric light curve evolution of our models for series A, B, and C, respectively. For each series, the models are grouped together with the explosion energy used in the `STELLA` simulation. The figures exhibit the differences in the morphology of the light curves based on the combination of the progenitor and the CSM properties. For the A-series (RSG) and B-series (YSG) models, we see a rise in the luminosity followed by a plateau phase characteristic of SN-IIP. The plateau phase lasts for 80-120 days, representing the recombination of hydrogen in the H-rich envelope, following which the luminosity drops until the radioactive tail is reached at around 100-140 days. The models with no CSM envelope show luminosity declining right after the initial shock breakout reaching a plateau phase. For the models that have a CSM envelope, the luminosity rises slowly after the initial shock-breakout and reaches a maximum in luminosity at a few tens of days. The rise time to the peak, the peak luminosity, and the decline time after the peak to reach the plateau phase increase with increasing CSM mass. As expected, the higher explosion energy produces brighter light curves. Peak luminosities of a few times $10^{42} - 10^{43}$ erg s^{-1} , typical of both standard Type II_n SNe but also more luminous SLSN-II are reached for these models.

For the C-series (BSG) models without CSM envelope, the light curves are morphologically similar to SN-Ib/c, showing a luminosity peak powered by the radioactive decay of ^{56}Ni after the initial shock breakout, followed by a steep decline. For the models with a CSM envelope, the energy deposited by the shocked CSM powers the light curve. The luminosity declines for 10-15

days, reaching a second peak around 10-20 days, which is when the radioactive decay of ^{56}Ni heats the underlying ejecta. The second peak for the models with larger CSM is brighter than the models with lower or no CSM, relative to their primary peak. These model light curves morphologically resemble those of the classical SN-Ib; however, the peak luminosities of both the primary and secondary peaks reach a few times $10^{43} - 10^{44}$ erg s^{-1} , typical of more luminous SLSN-I.

3.2. Spectroscopic evolution

The model spectra for the A- through C-series models are displayed in Figures 4 to 6, respectively. The spectra in Figures 4 & 5 are normalized to the continuum using the `Specutils` package ([Earl et al. 2022](#)) in Python. A generalized continuum is fitted in the range of 400-700 nm, excluding the region of strong emission lines. The figures show the evolution of spectra between 5 days to a few tens of days since the peak luminosity. In the models where the CSM envelope is absent, the hydrogen lines are broader as expected for rapidly expanding SN ejecta. As time progresses, the P Cygni profile developing for the lines can be observed in these models. This behavior is of course typical of SN IIP. The He lines also get stronger at this epoch due to the deeper layers of the ejecta being traced by the photosphere. The metal lines for iron and calcium start appearing in the spectra of these models at later times.

The Series A and Series B models with dense H-rich CSM winds exhibit strong, narrow hydrogen lines in their spectra, as is typical for SN II_n. The properties of the Balmer series hydrogen lines H_α and H_β are listed in Tables A1 and A2 for the A- and B-series models, respectively. The strength of the H_α and the H_β lines drop as time progresses. At any epoch relative to peak luminosity, the $F(H_\alpha)/F(H_\beta)$ ratio is higher for models with greater CSM mass compared to those with lower or no CSM. The models show similar trends in the time evolution of the two Balmer series hydrogen lines to the SN models of [Dessart et al. \(2016\)](#) that include the CSI, even though their CSM properties are vastly different (see, for example, the spectra of their model A in figure 5.) The strength of the lines diminishes as time progresses, eventually showing P-Cygni features at later times.

Figure 7 shows $F(H_\alpha)$ in the upper panel and the ratio of $F(H_\alpha)/F(H_\beta)$ in the lower panel, as calculated by the `SuperLite` code at the epoch closest to the peak bolometric luminosity for the A- and B-series models. Unlike models with lower ejecta mass and energy, those with higher ejecta mass and explosion energy exhibit narrow helium emission lines. This is because of the

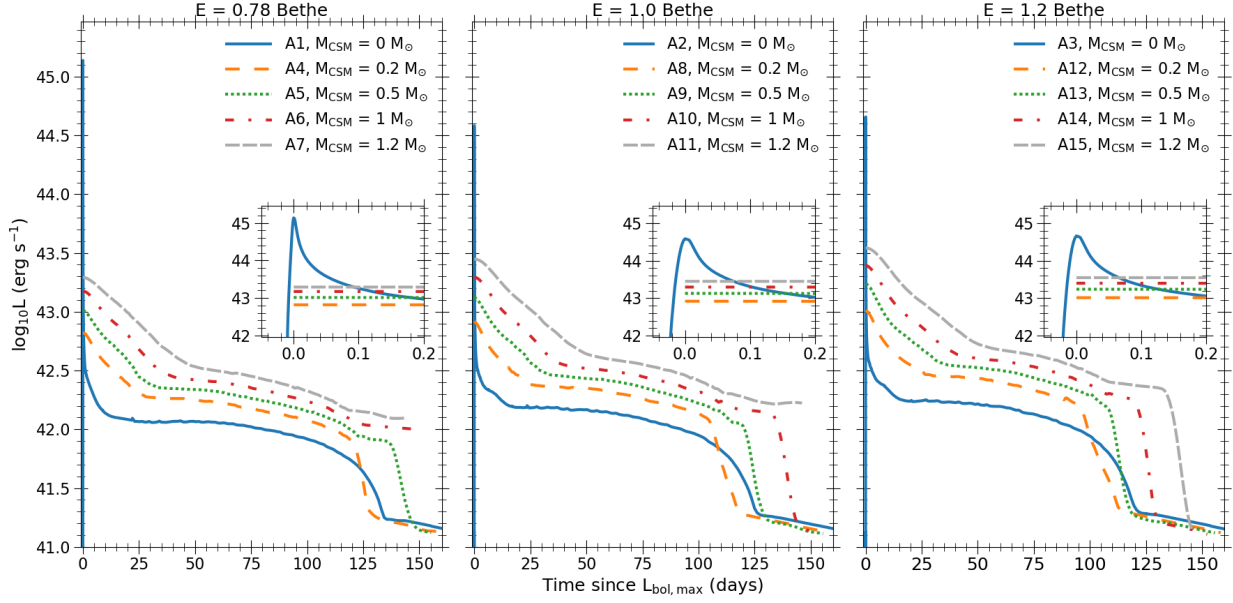


Figure 1. The light curves for the A-Series models representing RSG progenitors are shown here for a range of CSM masses and explosion energy values. The properties of the progenitor and the CSM for each of these models are listed in Table 1.

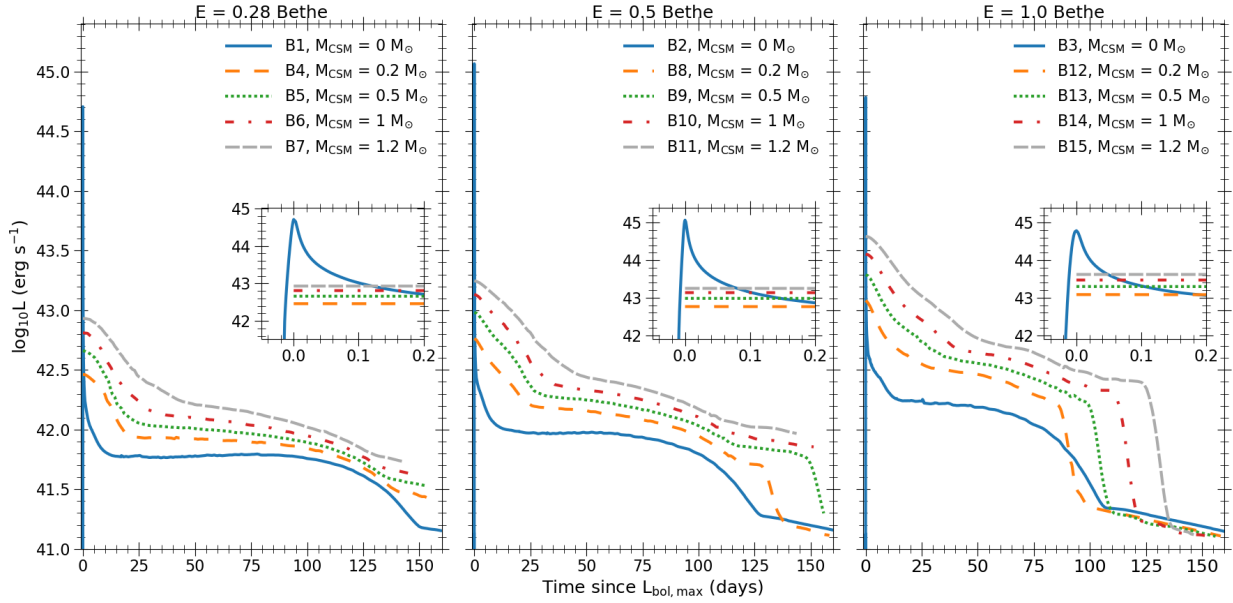


Figure 2. The light curves for the B-Series models representing YSG progenitors are shown here for a range of CSM masses and explosion energy values. The insets show light curves near the maximum value. The properties of the progenitor and the CSM for each of these models are listed in Table 1.

higher gas temperatures and stronger photoionization in these models, even though the ratio of H/He is the same between the models with different ejecta masses. The spectra for C-series models look more or less featureless in the optical region. The models with higher CSM mass show broad He lines in the spectra, which form in the

He-rich CSM envelope. The spectra seen in C-series models are consistent with the observations of the SLSN-I (Nicholl et al. 2016a,b; Quimby et al. 2018).

3.3. Statistical Analysis of the Balmer series H-lines

In this section, we present the results of the data analysis performed on the properties of the Balmer series

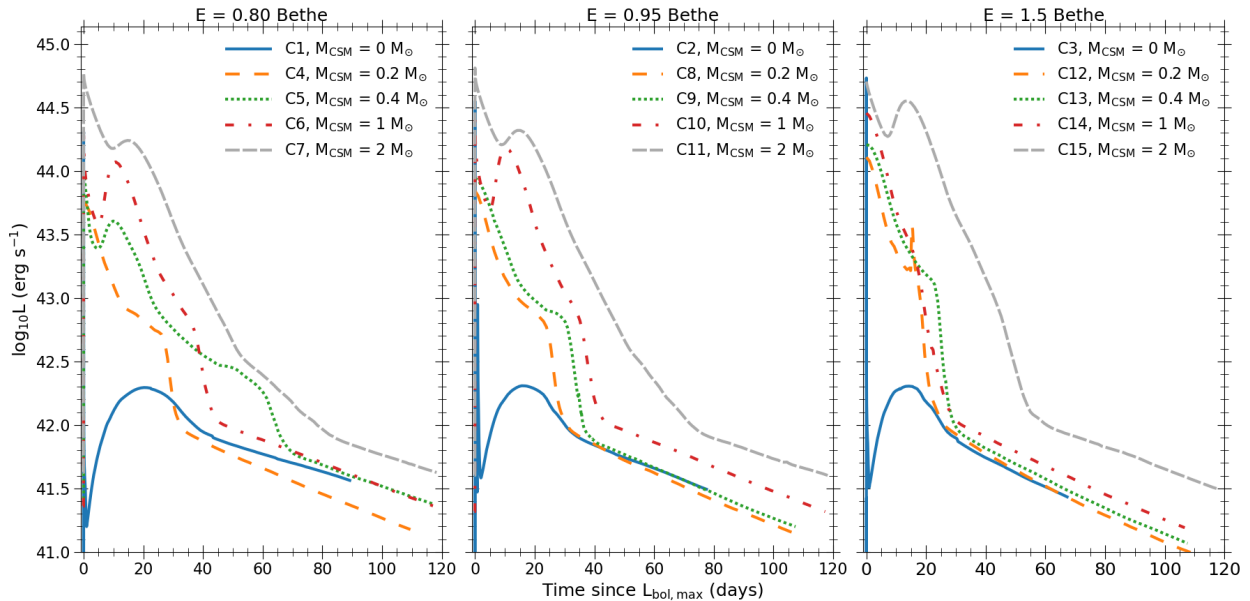


Figure 3. The light curves for the C-Series representing BSG progenitors models are shown here for a range of CSM masses and explosion energy values. The insets show light curves near the maximum value. The properties of the progenitor and the CSM for each of these models are listed in Table 1.

lines listed in Tables A1 and A2. The purpose of this analysis is to find correlations between the H line predictions from *SuperLite* code (hereafter, the targets) and the properties of the progenitor and the CSM (hereafter, the features) in a systematic manner. The properties listed in the table for H-lines include the amplitudes, fluxes, and line widths of the H_α and the H_β lines, and the ratio of the amplitudes and the fluxes for the two lines. The dimensionality of the targets and the features is reduced by finding the correlations within each of the two sets using a statistical method called Variance Inflation Factor (VIF, Neter et al. 1996) to detect the presence of multicollinearity within the features, and the same for the targets. It is a quantitative method that assesses the inflation of variance of the regression coefficient with other predictors. We use the Python package *StatsModel*³ for this method. A typical VIF score between 1.0 and 5.0 is acceptable. The features and targets that have scores higher than 10 are eliminated, in an iterative manner, starting with the highest scores, until the remaining features and targets have scores between 1.0 & 5.0. We find that the amplitudes, fluxes, and the line-widths of the H-lines are highly correlated. Thus, only the two uncorrelated quantities, the flux of H_α line $F(H_\alpha)$ and the ratio of the fluxes of the two lines, $F(H_\alpha)/F(H_\beta)$, are considered as the targets for further

analysis. Similarly, among the features, the uncorrelated quantities are the day since the peak luminosity, the explosion energy (E_{exp}), the radius of the progenitor at the time of the explosion (R_{exp}), the LTE/NLTE case, and the ratio of the ejecta mass to the that of the CSM ($M_{\text{ej}}/M_{\text{CSM}}$).

After eliminating the highly correlated quantities, we employ the technique of a simple machine learning algorithm called K-Nearest Neighbors (KNN, Cover & Hart 1967), where the targets are classified based on the proximity or the average value of their k nearest neighbors in the features space. The performance of our machine learning algorithm is evaluated using cross-validation techniques, where a part of the data is used for training the model and the rest is used to test its performance. The process is repeated until an optimized value of the mean squared error is achieved. We use the Python package *SKLearn* (Pedregosa et al. 2011) for this analysis.

The results of the KNN analysis performed on the data for the targets and the features are displayed in Figure 8. Panel (a) of the figure shows the ranked absolute feature importance scores for $F(H_\alpha)$, and panel (b) shows the same for the ratio $F(H_\alpha)/F(H_\beta)$. The feature importance score is an assessment of the model’s performance following the perturbation of a specific feature. For a given model, the higher importance score implies that the said feature is more important in determining the value of the target. The scales for different models

³ <https://github.com/statsmodels/statsmodels>

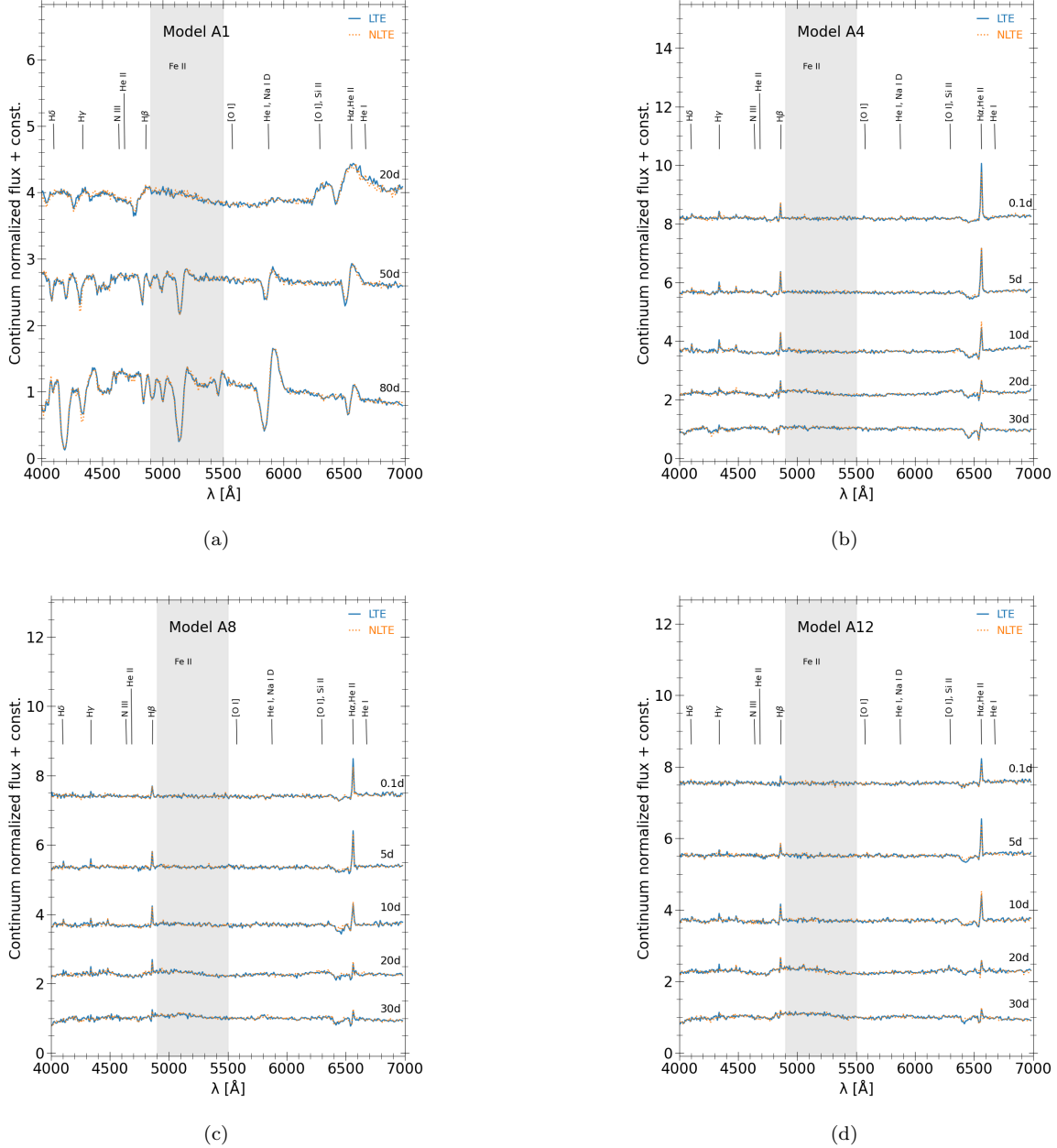


Figure 4. The time evolution of spectra produced by the SuperLite code for some of the A-Series models representing RSG progenitors is shown here. The properties of these models are listed in Tables 1 & A1. Model A1 where the CSM is absent shows typical P-Cygni lines of hydrogen for the phases representing the plateau phase of the light curve, while the other models where the CSM is present show strong emission lines of hydrogen, which diminish in strength as time progresses.

do not compare directly due to the differences in the model type, error metrics used, and data distribution. The KNN analysis for $F(H_\alpha)$ gives the optimal k -value of 4 with root mean squared error (RMSE) of 0.33. The radius R_{exp} and the ratio $M_{\text{ej}}/M_{\text{CSM}}$ are the most important features for the flux of the H_α line. The other features are comparatively less significant, according to the analysis. The H_α line flux correlates with R_{exp} , while

it anti-correlates with the ratio $M_{\text{ej}}/M_{\text{CSM}}$. In the case of the ratio $F(H_\alpha)/F(H_\beta)$, the optimal k -value is 2 with RMSE of 0.86. In this case, The radius R_{exp} again has the highest importance, followed by the LTE/NLTE case and the explosion energy E_{exp} . The ratio of the fluxes is anti-correlated with R_{exp} .

The combination of the dense CSM and higher velocity, higher mass ejecta leads to the formation of stronger,

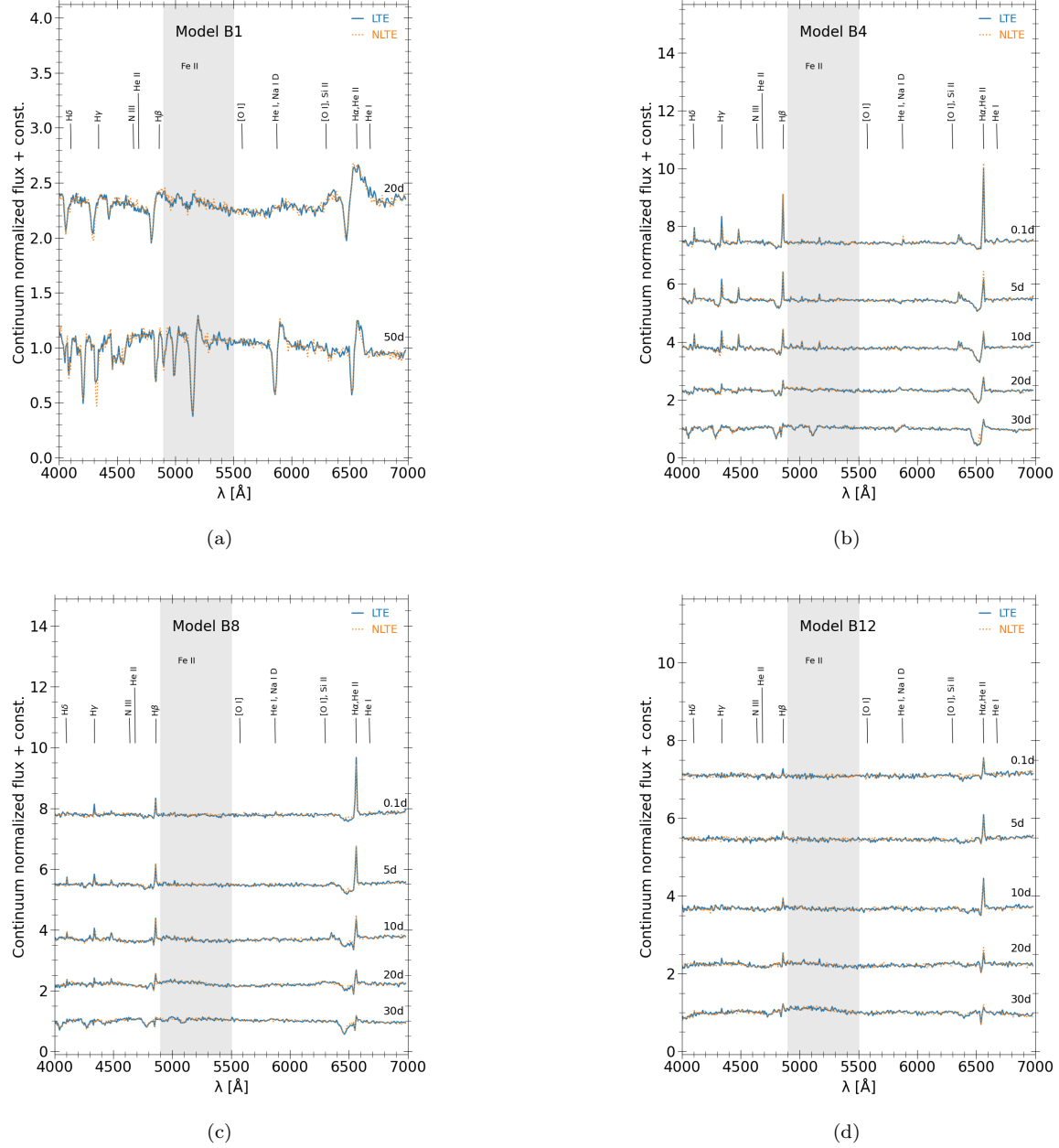


Figure 5. The time evolution of spectra produced by the SuperLite code for some of the B-Series models representing YSG progenitors is shown here. The properties of these models are listed in Tables 1 & A2. Model B1 where the CSM is absent shows typical P-Cygni lines of hydrogen, while the other models where the CSM is present show strong emission lines of hydrogen similar to A series models shown in Fig. 4

narrower emission lines of hydrogen due to higher densities and temperatures in the emitting region, which leads to more photoionization and in turn, more recombination as the gas cools down. As time progresses past the maximum luminosity, the photosphere recedes. The weaker recombination and the opacity effects reduce the flux in the H_α line, reducing the ratio $F(H_\alpha)/F(H_\beta)$. On the other hand, the lower velocity ejecta result in

weaker, broader emission lines due to lower temperatures in the interaction region. It can be seen in tables A1 & A2 that the line ratio gets stronger for the NLTE case, in comparison to the LTE case for calculation of the ionization states and excitation level population of hydrogen. It signifies that the NLTE conditions in the emitting region affect the H_α line, making it more prominent. Both the H_α line strength and the

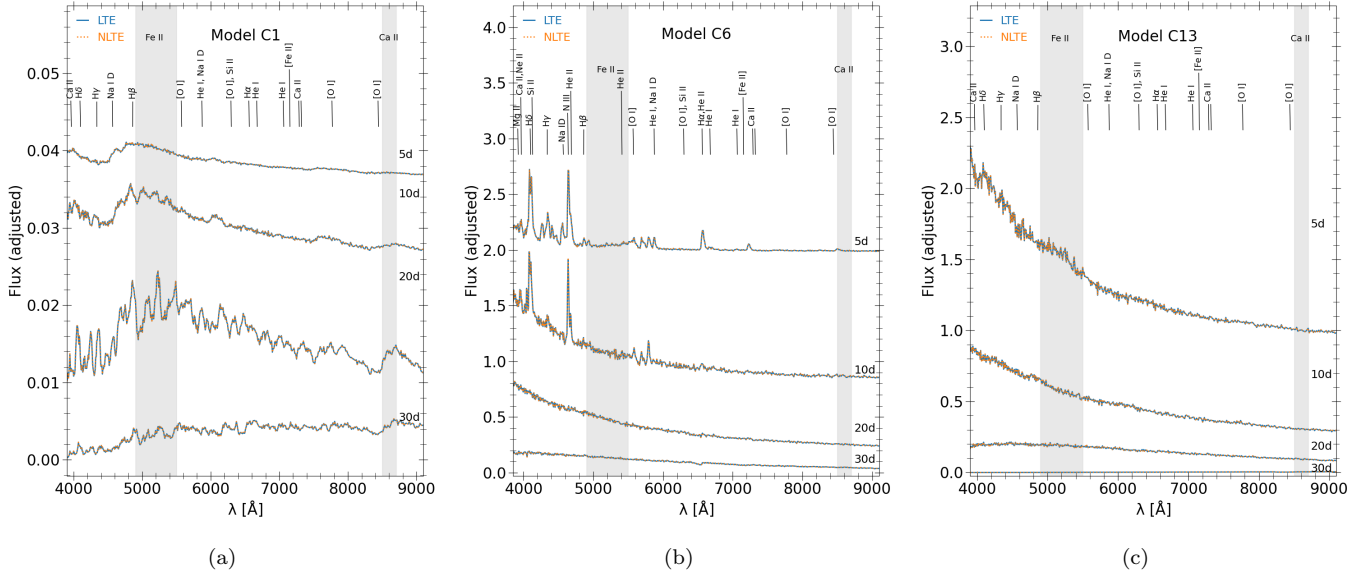


Figure 6. The time evolution of spectra produced by the SuperLite code for some of the C-Series models representing BSG progenitors is shown here. The properties of these models are listed in Tables 1. As hydrogen is absent in the ejecta and CSM of the C-series models, the NLTE treatment for hydrogen does not affect the results. The NLTE model spectra are included to emphasize the absence of hydrogen lines in the spectra

ratio $F(H_\alpha)/F(H_\beta)$ are higher near the peak luminosity. The peak in the luminosity signifies the highest ionization due to stronger shock heating. As the shock moves outward and the density of the CSM decreases, the flux of the H_α line and the ratio of the two lines decrease, and the lines become broader.

3.4. Comparisons Against Observed Spectra

To compare the SuperLite models against observations, we utilized Duplicated Superfit in Python, or Duperfit (Baer 2024). This program follows the same algorithm as Superfit by D. Andrew Howell (Howell et al. 2005) to evaluate an input spectrum against observed template spectra. In essence, an observed spectrum at observed redshift z , $o(\lambda; z)$, is considered to be a combination of supernova and host galaxy light. While best practice dictates that host galaxy modeling should remove galaxy contamination in SN spectra, this is not always done for SNe, particularly those in hosts with no archival spectra.

Superfit assumes the intrinsic SN spectrum to match some archival template, $t(\lambda; z)$, along with a host galaxy, $g(\lambda; z)$, both at the same redshift. To further emulate host galaxy modeling, the algorithm considers the total extinction in the V band, A_V , extinction parameter, $R_V \equiv A_V/E(B-V)$, and wavelength-specific extinction, $A(\lambda; R_V)$, given by a Cardelli law (Cardelli et al. 1989), to define a relative reddening $r(\lambda; R_V) \equiv A(\lambda; R_V)/A_V$, for which R_V is fixed to a user-defined value (3.1 by de-

fault) and A_V is a free fitting parameter. The equation of the model to fit the observed spectrum, then, is

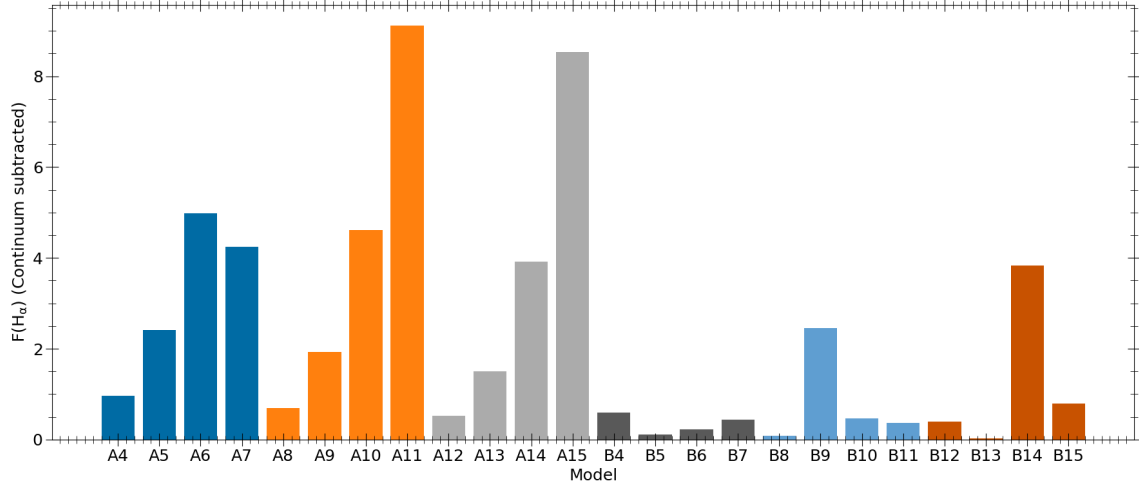
$$o_{\text{mod}}(\lambda; z) = Ct(\lambda; z)10^{-0.4A_V r(\lambda; z)} + Dg(\lambda; z) \quad (1)$$

for which C and D are free scaling parameters for fitting. The redshift z may be either fixed or free as a grid-search parameter. This model is then fitted via a method of least squares, where weights may be equal or provided by inverse variance (from error flux), or a weight spectrum that removes known telluric lines, or with a user-provided weight file. For our fits, we instructed Duperfit to estimate error flux using an iterative B-spline fit and to apply the inverse variance.

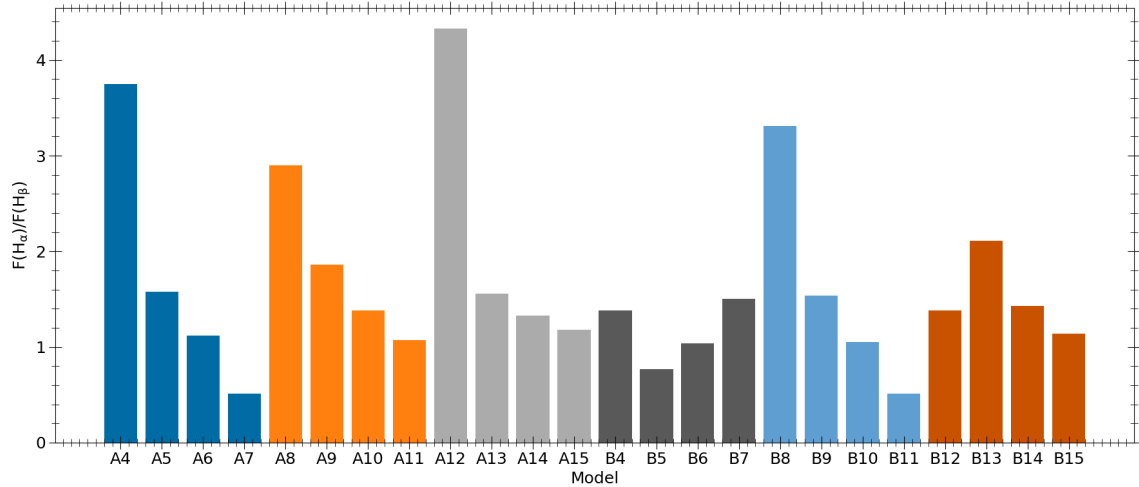
To better evaluate the spectral type, Duperfit further utilizes a semi-automated scoring mechanism devised by Quimby et al. (2018), referred to as mean-index difference (MID) scoring within the program. The program returns matched templates in order from best to worst and assigns indexes I to them from 0 to the total number of templates in that order. The program then computes a mean of the indices of the top 5 results of a given supernova type X, $\langle I_X \rangle$, repeats the same process for a type Y, $\langle I_Y \rangle$, then computes the difference:

$$\Delta I_{X-Y} = \langle I_X \rangle - \langle I_Y \rangle. \quad (2)$$

where more negative values imply stronger agreement with type X, and more positive values imply stronger agreement with type Y. Values near zero suggest ambiguity.



(a)



(b)

Figure 7. The top panel shows $F(H_\alpha)$ and the bottom panel shows the ratio of $F(H_\alpha)/F(H_\beta)$ for the A-series (RSG) and B-series (BSG) models for the epoch closest to the maximum in the bolometric light curve. Each set of models with the same explosion energy with increasing CSM mass is shown in the same color. As seen in the figure, there is a correlation between $F(H_\alpha)$ and the CSM mass, while the ratio of $F(H_\alpha)/F(H_\beta)$ shows an anti-correlation. The properties of these lines for the models are listed in Tables 1 & A1.

To evaluate the best method for evaluating SuperLite spectra with Duperfit, we tested a successful Type Ia model generated by SuperLite to assess how well it could be recaptured by the program. We tested two different schemes for evaluating the model spectra. Across both schemes, we fitted the supernova template scaling factor ($0.01 \leq C \leq 3$) and a relative extinction ($-4.5 \leq A_V \leq 2$) to account for any intrinsic reddening in specific supernova templates or color differences between SNe. The two schemes were then differentiated as follows:

- R1: Evaluate the spectrum at zero redshift with zero host galaxy emission modeled (i.e., the galaxy scaling factor D was fixed to zero)
- R2: Artificially redshift the spectra to $z = 0.1$, add a random amount of host galaxy emission to the input spectra via an Sc template, and set an Sc galaxy emission term to a free parameter (i.e., fit for $0 \leq D \leq 3$), and perform a redshift grid-search with $0.03 \leq z \leq 0.17$ with step size $\Delta z = 0.01$.

Table 2. A table of MID scores, ΔI_{X-Y} , for the SN Ia model spectrum with the two sets of fitting parameters is provided. Rows represent type X, and columns represent type Y. Scores of identical types, ΔI_{X-X} , are intentionally left blank as they provide no information.

		SNIa	SNIb	SNIc	SNII	SNIIn	SLSN-I
R1	SNIa	–	-179.0	-41.8	5.6	27.8	-26.2
	SNIb	179.0	–	137.2	184.6	206.8	152.8
	SNIc	41.8	-137.2	–	47.4	69.6	15.6
	SNII	-5.6	-184.6	-47.4	–	22.2	-31.8
	SNIIn	-27.8	-206.8	-69.6	-22.2	–	-54.0
	SLSN-I	26.2	-152.8	-15.6	31.8	54.0	–
R2	SNIa	–	-843.6	-622.8	-602.2	-474.2	-444.0
	SNIb	843.6	–	220.8	241.4	369.4	399.6
	SNIc	622.8	-220.8	–	20.6	148.6	178.8
	SNII	602.2	-241.4	-20.6	–	128.0	158.2
	SNIIn	474.2	-369.4	-148.6	-128.0	–	30.2
	SLSN-I	444.0	-399.6	-178.8	-158.2	-30.2	–

Evaluating these models in this way produces output from the program, as shown in Table 2. Note that the off-diagonal elements are antisymmetric, so the ordering of scores is relatively inconsequential. Thus, the program may roughly determine a best-matched SN type by finding the maximum absolute median value of the rows or columns.

Numerically, we more readily recapture the model as an SNIa using the R2 parameters. However, to better highlight this distinction, we also plot the scores alongside the scoring of the template library. The template library contains default evaluations in Duperfit, where the code intentionally ignores matching spectra of the same supernova. These scores are then plotted in a symmetrical logarithmic scale to show the distinction between score populations. For these plots, the best-matched type for the input model is assigned type X, and all other types are assigned type Y. The comparison is visible in Fig. 9.

With the results from both tests, we determined that the R2 parameters provide the best approach for evaluating the SuperLite spectra. For each series, we chose models 1, 5, 9, and 13 to match explosion energy and noted the differences as CSM mass increased. We then used the MID scoring included in Duperfit to compute the best-fit empirical match of spectral type to these models.

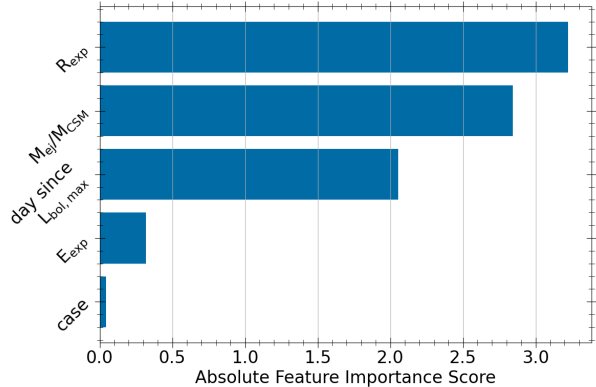
The A1 model strongly agrees with non-interacting SNe II, while each increasing CSM mass model correlates more strongly with SNe IIn. The A5 model becomes more consistent with SNe II after 50 days from maximum light. We can see this evolution in A5 by com-

paring its best match at 10 days to 50 days past maximum, the Type IIn SN 2005kj and Type II SN 2004dj, respectively, in Fig. 10.

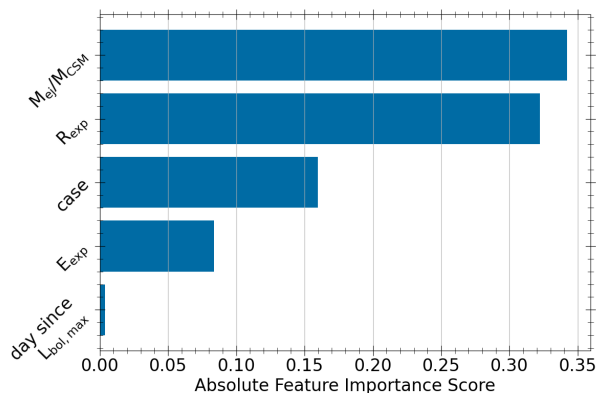
The B1 model strongly correlates with SNe II, while the B5 model’s best match was ambiguous between SNe II, IIn, and Ic. We can see in Fig. 10 that, at the scored Ic-like phase 5 days past maximum light, the best-matched result remains the Type IIn SN 1995G with some strong convergence. The remaining B-series models are more consistent with SNe IIn up to the 50 days past maximum light in their evolutionary modeling.

The fitting of the C1 model was, curiously, ambiguous between SNe II, IIn, and Ic. This is likely due to Duperfit, like Superfit before it, numerically determining a best fit of the spectrum without regarding particular identifying features. In Fig. 10, we show the best-matched spectrum against the artificially reddened and galaxy-contaminated spectrum, using the fitted parameters. While the general shape has converged to a good fit, the features do not necessarily align.

The C5 model showed consistency with hydrogen-deficient SLSNe, though its early phases’ top results did not converge to satisfactory goodness-of-fit values. However, 30 days past maximum light, the constraint improves significantly, as shown in Fig. 10, where the second-best match for the LTE model and the best match for the NLTE model closely resemble the Type I SLSN 2010gx at 10 days past maximum light. Note, in particular, the similarity of the LTE model continuum to the O II absorption features in the 4000-4700Å range, which Quimby et al. (2018) identified as unique



(a)



(b)

Figure 8. The figure shows the ranked absolute feature importance scores for the K-nearest neighbor (KNN) analysis performed on the flux of the H_α line, $F(H_\alpha)$ in the panel (a), and the ratio $F(H_\alpha)/F(H_\beta)$ in the panel (b).

characteristic distinguishing early-phase SLSNe-I. However, the poor physical representation of CSM interaction in LTE models means that this match should be treated with some scrutiny.

Finally, C9 and C13 had the best fits with SNe IIn in their scores. While the C-series models lacked H lines in their spectra, Superfit (and, by extension, Duperfit) does not weigh line presence more heavily than other features when evaluating the best fit. Furthermore, the template library of SNe IIn is fairly heterogeneous, including events of weaker H-line strength. For instance, the C9 model at 30 days had a best match with the Type IIn SN 2008fq, which itself had fairly weak lines. Finally, some higher-ranked matches for certain spectra had a higher-scaled galaxy template over the SN template, which may skew that result.

4. CONCLUSIONS

In this study, we explored the question of whether the observed diversity in supernovae (SNe) and superluminous supernovae (SLSNe) can be attributed to the diversity in the circumstellar material (CSM) surrounding massive stars. Our analysis was based on three model series – A, B, and C – each associated with different types of single star progenitors: a red supergiant (RSG), a yellow supergiant (YSG), and a blue supergiant (BSG). These progenitors were evolved using the MESA code, and the subsequent SN ejecta were simulated using the hydrodynamic code STELLA. The evolution profiles generated by STELLA were further processed with the Monte Carlo radiation transport code SuperLite to derive the spectral evolution at various epochs.

- **Influence of CSM Mass and Composition:** We found that the mass and composition of the CSM are critical in determining the type of SN, as expected. Specifically, our models suggest that the presence and richness of the CSM influence both the spectral class and light curve characteristics of the resultant transient, as well as its specific spectral evolution, particularly in terms of the relative strengths of the H_α and H_β lines.
- **Spectral Diversity Across Models:**
 - Models with RSG and YSG progenitors typically resembled SN-IIP in the absence of a CSM envelope but transitioned to SN-IIIn and SLSN-II profiles when an H-rich CSM was present.
 - BSG progenitors, due to their compact nature, predominantly produced light curves and spectra similar to SN-Ib/c. In scenarios with a He-rich CSM, the models predicted brighter light curves, characteristic of some SLSN-I events.
- **Line Strength and Flux Ratios:** Our analysis highlighted a correlation between the progenitor properties (such as radius at explosion) and the CSM characteristics (e.g., mass ratio of ejecta to CSM) with the observed strengths and ratios of Balmer series lines, particularly H_α and H_β . Notably:
 - The strength of H_α was significantly greater in models with larger progenitor radii and thicker H-rich CSM layers, indicating a stronger interaction and greater hydrogen ionization.
 - Conversely, H_β was relatively stronger in configurations with higher explosion energies and less dense CSM, suggesting different excitation conditions.

Our findings provide valuable insights into how the physical characteristics of progenitors and their surrounding CSM contribute to the spectroscopic evolution

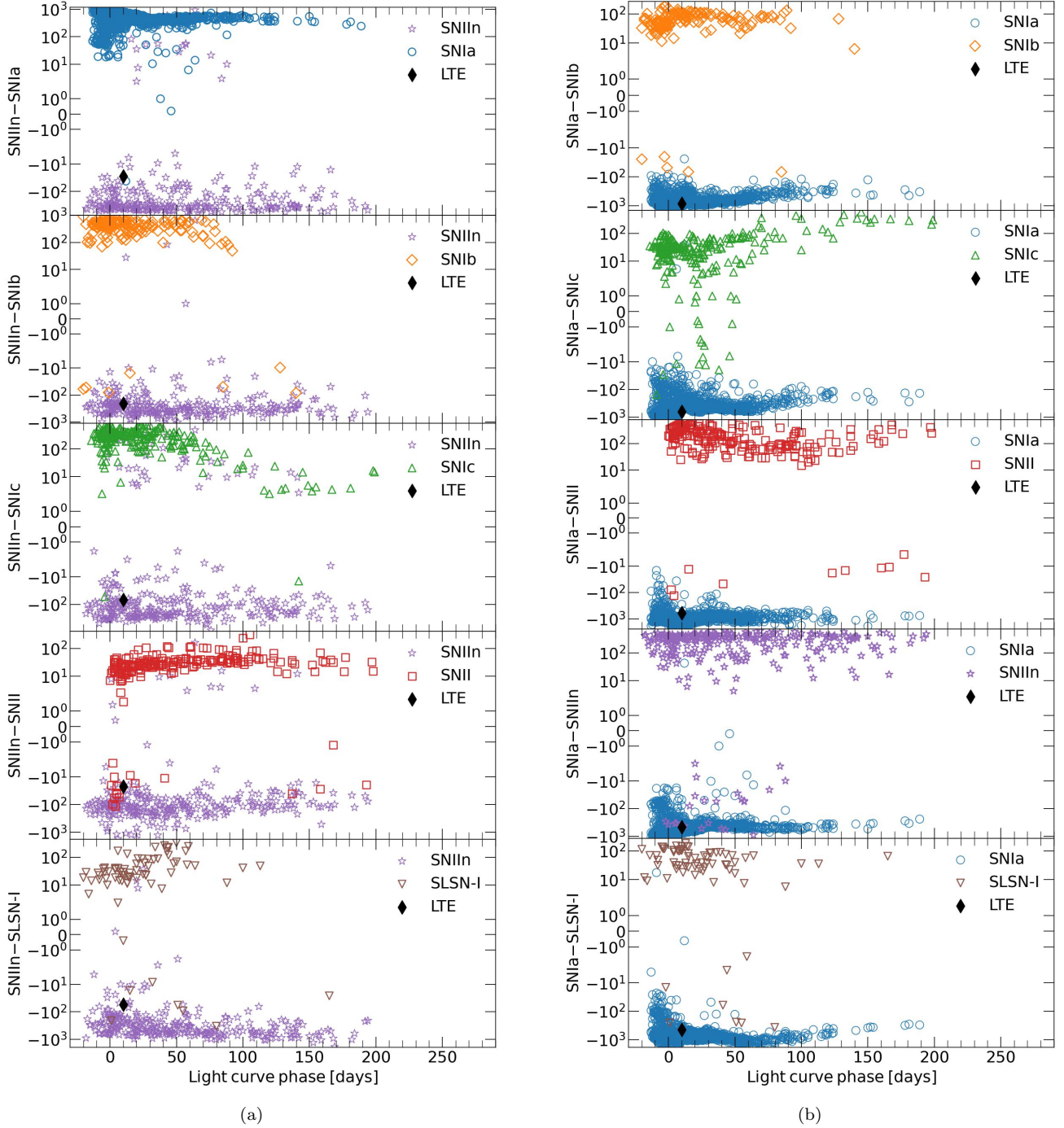


Figure 9. MID score distributions for the SN Ia model fit are shown to visualize the scoring method. The fitting was performed to verify that the chosen fitting scheme reproduces a well-determined spectral type for a given model. Colored populations represent the template library’s evaluations as a comparison set, while the black rhombus represents the input spectrum. The first type across the subplots represents the numerically best-matched type. Plots are symmetric-logarithmically scaled to clearly show the numerical separation between populations. (a) Distributions representing the fit with the R1 scheme. (b) Distributions representing the fit with the R2 scheme.

of these transients. The strength and ratio of Balmer lines, as influenced by various model parameters, offer

a promising method for inferring progenitor and CSM properties from observed spectra.

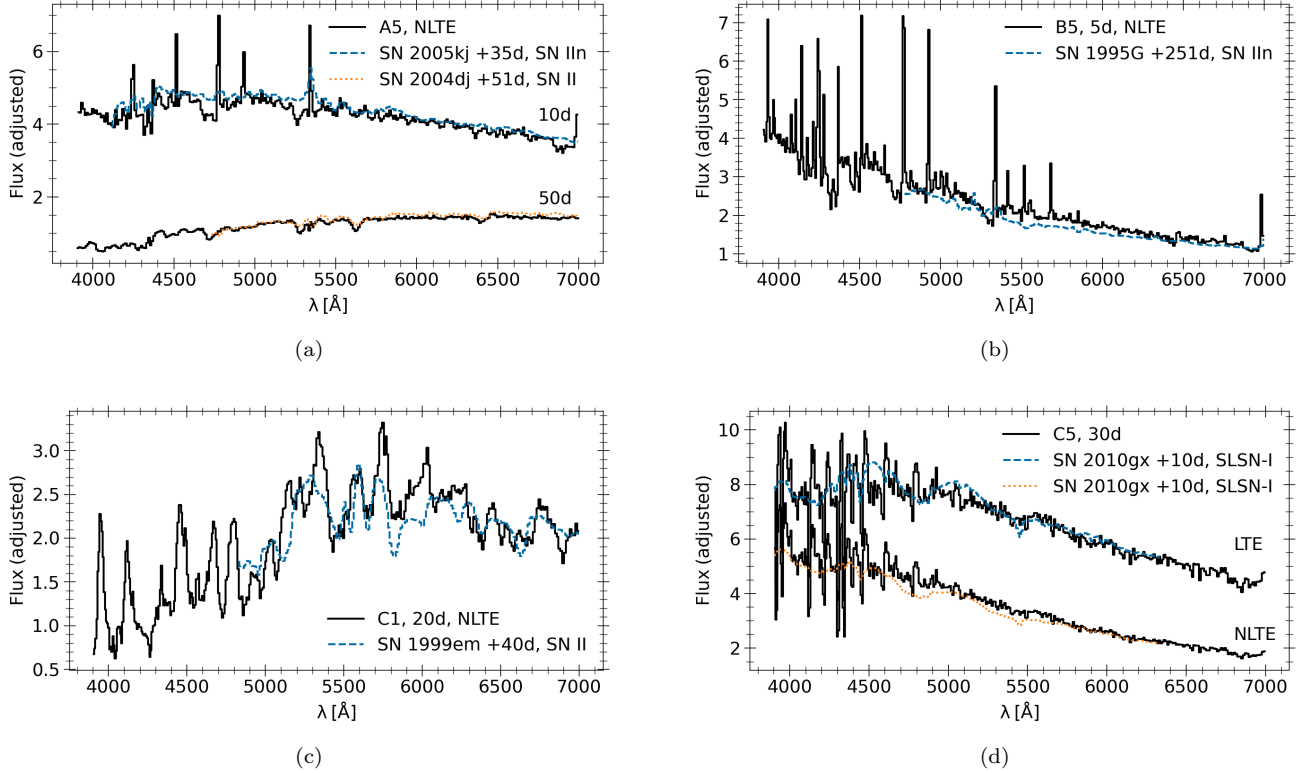


Figure 10. Plots of artificially reddened and galaxy-contaminated spectra for various models and the Duperfit-determined best-fit template model representing strong type correlation for the given phase. (a) The NLTE A5 model against Duperfit’s best matches at 10 and 50 days, (b) the NLTE B5 model against its best match at 5 days, (c) the NLTE C1 model against Duperfit’s best match at 20 days, and (d) the LTE C1 model against Duperfit’s second-best match at 30 days and the NLTE C1 model against Duperfit’s best match at 20 days.

Looking ahead, we aim to extend this research to hydrogen-poor events, exploring a broader range of parameters, such as different CSM shapes and geometries, using advanced simulations with SuperLite. This expansion could potentially unveil further nuances in the spectroscopic signatures of luminous transients, enhancing our understanding of their progenitors and explosion mechanisms.

Software: SuperNu(Wollaeger et al. 2013; Wollaeger & van Rossum 2014), SuperLite (Wagle et al. 2023; Wagle 2023), Duperfit (Howell et al. 2005; Baer 2024), STELLA (Blinnikov & Bartunov 1993; Blinnikov et al. 1998; Blinnikov & Sorokina 2004; Blinnikov et al. 2006), MESA r-15140 (Paxton et al. 2011, 2013, 2015, 2018, 2019), NumPy (Harris et al. 2020), Pandas (McKinney et al. 2010), Astropy (Astropy Collaboration et al. 2022; Price-Whelan et al. 2018), Specutils (Earl et al. 2022), SKLearn (Pedregosa et al. 2011)

1 We would like to thank Ryan Wollaeger, J. Craig
 2 Wheeler, Chris Fryer and Nathan Smith for useful dis-
 3 cussions. G.W would like to thank Michael Attia for his
 4 valuable inputs on the ML techniques for data analysis.
 5 G.W. and E.C. would like to thank the National Sci-
 6 ence Foundation (NSF) for their support made possible
 7 by the NSF grant AST-1907617. EC would also like to
 8 thank NASA and the Smithsonian Astrophysical Obser-
 9 vatory (SAO) for their support via the Chandra X-ray
 10 Observatory (CXO) theory grant TM4-25003X.

A. APPENDIX A

Table A1. Hydrogen Line Properties for A Series Models.

Model	day since $L_{\text{bol,max}}$	L_{bol} ($\times 10^{42}$)	H-Opacity	$A(H\alpha)_{CN}$	$A(H\alpha)_{CS}$ ($\times 10^{-2}$)	$F(H\alpha)$ ($\times 10^{-1}$)	$EW(H\alpha)$	$A(H\beta)_{CN}$	$A(H\alpha)_{CS}$ ($\times 10^{-2}$)	$F(H\beta)$ ($\times 10^{-1}$)	$EW(H\beta)$	$A(H\alpha)_{CN}/$ $A(H\alpha)_{CS}$	$F(H\alpha)/$ $F(H\beta)$
(1)	(2)	(3)	(4)	(5)	(6)	(7)	(8)	(9)	(10)	(11)	(12)	(13)	(14)
A4	0.1	5.82	LTE	2.82	6.61	9.66 ± 1.37	-26.59	1.52	2.87	2.58 ± 1.17	-4.63	1.86	3.75
			NLTE	2.50	5.47	7.68 ± 1.24	-21.09	1.55	3.07	2.68 ± 1.18	-4.83	1.61	2.87
	5	4.18	LTE	2.47	4.38	6.69 ± 1.02	-22.50	1.73	3.35	3.42 ± 1.04	-7.44	1.43	1.95
			NLTE	2.51	4.48	6.29 ± 1.01	-21.17	1.69	3.16	3.30 ± 1.03	-7.18	1.49	1.91
A5	10	3.09	LTE	1.76	1.81	2.45 ± 0.62	-10.32	1.68	2.51	2.40 ± 0.82	-6.47	1.05	1.02
			NLTE	1.96	2.30	3.22 ± 0.68	-13.52	1.65	2.44	2.50 ± 0.83	-6.71	1.19	1.29
	20	1.94	LTE	1.42	0.66	0.92 ± 0.36	-5.85	1.43	1.08	0.80 ± 0.52	-3.15	1.00	1.15
			NLTE	1.45	0.71	0.93 ± 0.37	-5.88	1.36	0.90	0.58 ± 0.51	-2.29	1.07	1.60
A6	0.1	9.36	LTE	3.86	15.3	24.1 ± 2.70	-45.24	2.75	15.5	15.3 ± 2.59	-17.20	1.41	1.58
			NLTE	3.80	14.8	22.6 ± 2.61	-42.64	2.67	14.8	14.2 ± 2.53	-15.95	1.42	1.60
	5	7.28	LTE	2.56	7.39	11.8 ± 1.70	-24.84	2.73	13.5	12.0 ± 2.23	-15.32	0.94	0.99
			NLTE	2.84	8.73	13.7 ± 1.84	-28.90	2.70	13.2	11.8 ± 2.20	-15.28	1.05	1.16
A5	10	5.34	LTE	1.90	3.55	4.71 ± 1.08	-11.96	2.37	8.68	7.51 ± 1.65	-11.86	0.80	0.63
			NLTE	2.07	4.19	5.73 ± 1.15	-14.61	2.34	8.44	8.28 ± 1.67	-13.10	0.89	0.69
	20	3.26	LTE	1.65	1.82	1.98 ± 0.68	-7.09	1.48	2.03	1.60 ± 0.87	-3.79	1.11	1.24
			NLTE	1.68	1.89	2.16 ± 0.69	-7.77	1.45	1.91	1.65 ± 0.87	-3.93	1.16	1.31
A6	0.1	14.3	LTE	5.53	29.4	49.8 ± 4.64	-76.60	4.51	43.3	44.4 ± 5.32	-35.90	1.23	1.12
			NLTE	5.57	29.9	51.6 ± 4.74	-78.85	4.38	41.8	$42/7 \pm 5.20$	-34.61	1.27	1.21
	10	9.08	LTE	2.82	10.4	16.6 ± 2.21	-29.22	3.13	21.2	21.2 ± 2.33	-21.23	0.90	0.79
			NLTE	2.87	10.7	17.1 ± 2.24	-29.91	3.06	20.4	21.4 ± 3.17	-21.59	0.94	0.80
20	5.78	LTE	2.14	5.17	7.28 ± 1.37	-16.09	1.75	5.59	4.24 ± 1.65	-5.69	1.23	1.72	
		NLTE	2.2	5.39	7.38 ± 1.39	-16.41	1.78	5.83	4.21 ± 1.66	-5.64	1.23	1.75	

Table A1 continued

Table A1 (continued)

Model	day since $L_{\text{bol,max}}$	L_{bol} ($\times 10^{42}$)	H-Opacity	$A(H_{\alpha})_{CN}$	$A(H_{\alpha})_{CS}$ ($\times 10^{-2}$)	$F(H_{\alpha})$ ($\times 10^{-1}$)	$EW(H_{\alpha})$	$A(H_{\beta})_{CN}$	$A(H_{\alpha})_{CS}$ ($\times 10^{-2}$)	$F(H_{\beta})$ ($\times 10^{-1}$)	$EW(H_{\beta})$	$A(H_{\alpha})_{CN}$	$F(H_{\alpha})/$ $F(H_{\beta})$
(1)	(2)	(3)	(4)	(5)	(6)	(7)	(8)	(9)	(10)	(11)	(12)	(13)	(14)
A7	0.1	19.9	LTE	3.75	17.3	42.5±4.02	-58.49	5.95	77.9	83.3±8.81	-52.97	0.63	0.51
			NLTE	7.67	48.8	87.3±7.24	-119.05	5.77	74.7	79.4±8.51	-50.66	1.33	1.10
	5	17.6	LTE	2.77	11.3	28.2±3.25	-36.23	4.45	54.8	59.1±6.96	-37.14	0.62	0.48
			NLTE	3.83	22.0	43.2±4.25	-54.48	4.41	54.3	57.4±6.89	-36.03	0.87	0.75
	10	14.4	LTE	2.25	85.4	18.1±2.57	-24.24	3.33	33.2	34.6±4.91	-24.21	0.68	0.52
			NLTE	3.84	21.4	39.1±3.98	-51.85	3.26	32.6	34.5±4.89	-23.98	1.18	1.13
A8	20	9.71	LTE	2.70	10.8	17.9±2.40	-28.17	2.07	12.5	12.3±2.91	-10.49	1.31	1.46
			NLTE	2.85	11.8	19.4±2.52	-20.35	2.14	13.4	11.5±2.92	-9.80	1.33	1.69
	0.1	7.35	LTE	2.05	5.09	6.98±1.41	-14.49	1.31	2.24	2.41±1.47	-3.31	1.57	2.90
			NLTE	1.83	4.00	4.99±1.28	-10.32	1.29	2.14	2.11±1.46	-2.90	1.41	2.36
	5	5.04	LTE	2.05	3.92	5.50±1.10	-14.66	1.45	2.49	2.16±1.14	-3.91	1.41	2.54
			NLTE	1.97	3.63	4.86±1.06	-12.93	1.43	2.39	1.88±1.13	-3.42	1.37	2.58
A9	10	3.58	LTE	1.60	1.71	2.81±0.73	-9.77	1.55	2.22	2.04±0.86	-5.02	1.03	1.38
			NLTE	1.66	1.89	2.79±0.74	-9.74	1.50	2.02	1.68±0.84	-4.14	1.11	1.67
	20	2.27	LTE	1.31	0.58	0.50±0.40	-2.65	1.39	1.06	0.97±0.55	-3.57	0.94	0.52
			NLTE	1.39	0.73	0.68±0.41	-3.60	1.32	0.87	0.56±0.53	-2.08	1.05	1.20
	0.1	12.6	LTE	2.63	12.3	19.3±2.75	-25.71	1.92	11.3	10.4±2.89	-8.40	1.37	1.86
			NLTE	2.57	11.9	18.1±2.68	-23.98	1.77	9.48	8.60±2.78	-6.97	1.46	2.11
A9	5	9.12	LTE	2.35	8.42	12.8±2.06	-20.46	2.06	10.4	9.70±2.39	-9.88	1.14	1.31
			NLTE	2.49	9.25	13.4±2.12	-21.60	2.07	10.5	10.2±2.41	-10.37	1.20	1.32
	10	6.49	LTE	1.75	3.72	5.71±1.32	-11.57	2.11	8.37	7.20±1.85	-9.52	0.83	0.79
			NLTE	1.93	4.57	7.36±1.43	-14.94	2.09	8.18	7.55±1.84	-10.07	0.92	0.98
	20	4.07	LTE	1.40	1.42	1.64±0.79	-4.67	1.51	2.57	1.48±0.10	-2.97	0.93	1.11
			NLTE	1.46	1.59	1.63±0.71	-4.67	1.44	2.20	1.41±1.01	-2.81	1.01	1.16

Table A1 continued

Table A1 (continued)

Model	day since $L_{\text{bol,max}}$	L_{bol} ($\times 10^{42}$)	H-Opacity	$A(\text{H}\alpha)_{\text{CN}}$	$A(\text{H}\alpha)_{\text{CS}}$ ($\times 10^{-2}$)	$F(\text{H}\alpha)$ ($\times 10^{-1}$)	$\text{EW}(\text{H}\alpha)$	$A(\text{H}\beta)_{\text{CN}}$	$A(\text{H}\alpha)_{\text{CS}}$ ($\times 10^{-2}$)	$F(\text{H}\beta)$ ($\times 10^{-1}$)	$\text{EW}(\text{H}\beta)$	$A(\text{H}\alpha)_{\text{CN}}$	$F(\text{H}\alpha)$
(1)	(2)	(3)	(4)	(5)	(6)	(7)	(8)	(9)	(10)	(11)	(12)	(13)	(14)
A10	0.1	19.3	LTE	4.09	27.8	46.1±4.87	-51.11	3.02	34.1	33.5±5.27	-19.87	1.35	1.38
			NLTE	4.03	27.3	45.7±4.83	-50.74	2.96	32.8	32.6±5.17	-19.50	1.36	1.40
	5	15.7	LTE	3.32	20.6	35.5±4.04	-40.03	2.85	29.0	30.9±4.78	-19.72	1.16	1.15
			NLTE	3.53	22.5	36.8±4.19	-41.53	2.85	28.9	28.8±4.71	-18.43	1.24	1.28
	10	11.1	LTE	2.55	11.2	18.1±2.59	-25.05	2.78	21.9	22.5±3.68	-18.28	0.92	0.80
			NLTE	2.65	11.9	19.2±2.66	-26.61	2.66	20.4	20.5±3.55	-16.69	1.00	0.94
A11	20	6.96	LTE	1.63	3.47	4.19±1.36	-7.59	1.74	6.43	4.75±1.90	-5.50	0.93	0.88
			NLTE	1.77	4.24	5.39±1.44	-9.79	1.64	5.58	4.30±1.87	-4.93	1.08	1.25
	0.1	27.8	LTE	6.18	51.1	91.2±7.95	-92.34	4.95	81.9	85.3±9.76	-41.13	1.25	1.07
			NLTE	6.21	51.5	94.5±8.10	-95.22	4.58	7.40	74.8±9.20	-37.91	1.36	1.20
	5	-24.6	LTE	3.33	24.2	46.9±5.00	-44.29	4.31	71.0	75.1±9.04	-34.99	0.77	0.62
			NLTE	5.00	42.6	78.3±7.14	-73.39	4.12	66.4	70.3±8.64	-33.00	1.21	1.11
A12	10	19.1	LTE	2.34	12.7	25.5±3.45	-26.42	3.47	46.7	50.8±6.79	-26.87	0.67	0.50
			NLTE	4.15	30.4	55.2±5.45	-57.12	3.61	49.3	53.0±6.97	-28.07	1.15	1.04
	20	11.9	LTE	2.15	9.02	15.1±2.49	-19.32	1.92	12.7	11.4±3.27	-8.27	1.12	1.32
			NLTE	2.23	9.75	16.4±2.59	-20.68	2.00	13.9	13.3±3.37	-9.56	1.11	1.24
	0.1	9.16	LTE	1.66	3.77	5.29±1.45	-9.33	1.22	1.93	1.22±1.73	-1.37	1.37	4.33
			NLTE	1.50	2.83	3.84±1.36	-6.73	1.15	1.36	1.35±1.72	-1.52	1.30	2.85
A12	5	6.03	LTE	2.01	4.36	5.77±1.24	-13.33	1.31	2.04	2.12±1.34	-3.19	1.54	2.72
			NLTE	1.87	3.74	5.05±1.18	-11.69	1.34	2.28	2.15±1.34	-3.26	1.39	2.35
	10	4.28	LTE	1.71	2.39	3.43±0.88	-10.19	1.46	2.30	2.15±1.04	-4.32	1.17	1.60
			NLTE	1.82	2.76	4.25±0.93	-12.63	1.41	2.03	2.01±1.03	-4.04	1.29	2.11
	20	2.78	LTE	1.33	0.75	0.96±0.51	-4.21	1.35	1.23	1.30±0.72	-3.71	0.98	0.74
			NLTE	1.34	0.79	0.63±0.44	-2.75	1.39	1.35	1.32±0.71	-3.81	0.97	0.48

Table A1 continued

Table A1 (continued)

Model	day since $L_{\text{bol,max}}$	L_{bol} ($\times 10^{42}$)	H-Opacity	$A(\text{H}\alpha)_{\text{CN}}$	$A(\text{H}\alpha)_{\text{CS}}$ ($\times 10^{-2}$)	$F(\text{H}\alpha)$ ($\times 10^{-1}$)	$\text{EW}(\text{H}\alpha)$	$A(\text{H}\beta)_{\text{CN}}$	$A(\text{H}\alpha)_{\text{CS}}$ ($\times 10^{-2}$)	$F(\text{H}\beta)$ ($\times 10^{-1}$)	$\text{EW}(\text{H}\beta)$	$A(\text{H}\alpha)_{\text{CN}}$	$F(\text{H}\alpha)/$ $F(\text{H}\beta)$
(1)	(2)	(3)	(4)	(5)	(6)	(7)	(8)	(9)	(10)	(11)	(12)	(13)	(14)
A13	0.1	16.2	LTE	2.11	9.79	15.0 \pm 2.70	-16.97	1.62	9.46	9.63 \pm 3.33	-6.35	1.30	1.56
			NLTE	2.05	9.29	14.1 \pm 2.64	-15.86	1.56	8.49	7.75 \pm 3.23	-5.12	1.31	1.81
	5	11.6	LTE	2.32	9.85	15.3 \pm 2.46	-20.52	1.79	9.61	10.1 \pm 2.81	-8.26	1.30	1.52
			NLTE	2.23	9.19	14.6 \pm 2.40	-19.58	1.81	9.95	9.08 \pm 2.79	-7.41	1.23	1.61
	10	7.80	LTE	1.86	4.85	7.46 \pm 1.58	-13.16	1.97	8.85	7.58 \pm 2.14	-8.34	0.94	0.98
			NLTE	2.07	6.06	9.04 \pm 1.69	-15.99	1.98	8.81	7.72 \pm 2.13	-8.56	1.05	1.17
	20	4.95	LTE	1.43	1.77	1.87 \pm 0.93	-4.53	1.57	3.55	2.60 \pm 1.30	-4.20	0.91	0.72
			NLTE	1.46	1.93	2.38 \pm 0.96	-5.73	1.59	3.61	2.92 \pm 1.31	-4.74	0.92	0.82
	0.1	24.0	LTE	3.12	22.4	39.2 \pm 4.60	-37.10	2.42	28.6	29.5 \pm 5.47	-14.69	1.29	1.33
			NLTE	2.97	20.8	35.2 \pm 4.35	-33.17	2.29	25.8	25.2 \pm 5.19	-12.64	1.29	1.40
A14	5	18.9	LTE	3.03	20.6	36.0 \pm 4.29	-35.54	2.61	2.94	28.1 \pm 5.15	-15.31	1.16	1.28
			NLTE	3.24	22.6	37.8 \pm 4.45	-37.45	2.43	26.4	27.8 \pm 5.06	-15.07	1.33	1.36
	10	13.1	LTE	2.63	13.3	23.1 \pm 3.07	-28.26	2.74	24.8	25.1 \pm 4.19	-17.62	0.96	0.92
			NLTE	2.69	13.8	22.5 \pm 3.07	-27.54	2.68	24.0	25.1 \pm 4.17	-17.55	1.00	0.90
	20	7.93	LTE	1.71	4.37	5.66 \pm 1.58	-9.18	1.81	8.00	6.78 \pm 2.24	-6.83	0.95	0.83
			NLTE	1.81	4.92	6.36 \pm 1.62	-10.42	1.73	7.24	6.53 \pm 2.22	-6.56	1.05	0.97
	0.1	34.7	LTE	5.00	45.4	85.4 \pm 7.68	-75.1	3.97	71.8	72.5 \pm 9.42	-30.00	1.26	1.18
			NLTE	4.90	44.2	83.7 \pm 7.56	-73.48	3.89	69.5	67.9 \pm 9.14	-28.18	1.26	1.23
	5	30.3	LTE	4.31	39.6	74.9 \pm 7.11	-62.21	3.58	64.1	68.9 \pm 9.05	-27.72	1.20	1.09
			NLTE	4.53	43.0	80.9 \pm 7.55	-66.33	3.55	63.6	65.7 \pm 8.94	-26.31	1.28	1.23
A15	10	23.2	LTE	2.81	19.5	39.7 \pm 45.8	-36.08	3.67	59.1	65.2 \pm 8.26	-29.49	0.77	0.61
			NLTE	4.40	37.6	69.3 \pm 6.62	-62.44	3.58	56.8	62.4 \pm 8.07	-28.35	1.23	1.11
	20	13.7	LTE	1.75	6.46	9.72 \pm 2.31	-11.21	2.27	20.1	20.6 \pm 4.17	-12.99	0.77	0.47
			NLTE	2.50	13.1	20.6 \pm 3.07	-23.57	2.21	19.2	21.1 \pm 4.17	-13.26	1.13	0.98

NOTE—The amplitudes have suffices CN and CS for continuum normalized and continuum subtracted spectrum, respectively. The continuum subtracted spectrum has a unit of $\text{erg cm}^{-2} \text{s}^{-1} \text{Å}^{-1}$. The line integrated flux in the units of $\text{erg cm}^{-2} \text{s}^{-1}$ is estimated using the line_flux routine from the Spectutils Python package.

Table A2. Hydrogen Line Properties for B Series Models.

Model	day	L_{bol} ($\times 10^{42}$)	H-Opacity	$A(H\alpha)_{CN}$	$A(H\alpha)_{CS}$ ($\times 10^{-2}$)	$F(H\alpha)$ ($\times 10^{-1}$)	$EW(H\alpha)$	$A(H\beta)_{CN}$	$A(H\alpha)_{CS}$ ($\times 10^{-2}$)	$F(H\beta)$ ($\times 10^{-1}$)	$EW(H\beta)$	$A(H\alpha)_{CN}/$ $A(H\alpha)_{CS}$	$F(H\alpha)/$ $F(H\beta)$	
(1)	(2)	(3)	(4)	(5)	(6)	(7)	(8)	(9)	(10)	(11)	(12)	(13)	(14)	
B4	0.1	2.56	LTE	3.51	4.22	6.05 ± 0.76	-35.93	2.73	4.34	4.37 ± 0.74	-17.40	1.29	1.38	
			NLTE	3.67	4.51	6.54 ± 0.80	-38.74	2.78	4.44	4.23 ± 0.73	-16.93	-16.93	1.32	1.55
	5	2.20	LTE	1.70	1.17	1.60 ± 0.43	-9.50	2.01	2.53	2.28 ± 0.60	-9.11	0.84	0.70	
			NLTE	1.97	1.62	2.29 ± 4.78	-13.70	2.03	2.55	2.52 ± 0.60	-10.19	-10.19	0.97	0.91
	10	1.65	LTE	1.49	0.67	7.31 ± 3.13	-5.41	1.66	1.32	1.32	1.33 ± 4.42	-6.71	0.90	0.55
			NLTE	1.58	0.78	0.92 ± 0.32	-6.86	1.69	1.36	1.36	1.20 ± 0.44	-6.10	0.94	0.77
20	0.74	LTE	1.46	2.97	4.22 ± 1.52	-6.53	1.34	3.17	3.17	2.10 ± 1.87	-2.24	1.09	2.01	
		NLTE	1.48	3.04	4.15 ± 1.51	-6.50	1.30	2.79	2.79	2.00 ± 1.86	-2.14	1.14	2.08	
0.1	4.25	LTE	3.69	7.01	1.08 ± 0.126	-41.60	4.33	1.41	1.41	1.41 ± 0.176	-33.31	0.85	0.77	
		NLTE	4.07	8.03	1.26 ± 0.138	-48.01	4.26	1.38	1.38	1.32 ± 0.172	-31.17	0.96	0.95	
5	3.77	LTE	2.37	3.63	5.08 ± 0.87	-19.20	2.42	6.06	6.06	5.06 ± 1.13	-11.84	0.98	1.00	
		NLTE	2.58	4.18	5.61 ± 9.15	-21.23	2.48	6.24	6.24	5.25 ± 1.13	-12.43	1.04	1.07	
10	2.53	LTE	2.39	2.78	3.72 ± 6.50	-18.60	1.83	2.63	2.63	1.87 ± 7.07	-5.93	1.30	1.99	
		NLTE	2.39	2.78	3.72 ± 6.50	-18.60	1.83	2.63	2.63	1.87 ± 7.07	-5.93	1.30	1.99	
20	1.10	LTE	1.65	6.31	8.16 ± 2.44	-8.34	1.31	4.47	4.47	3.41 ± 2.87	-2.37	1.26	2.39	
		NLTE	1.69	6.76	7.49 ± 2.43	-7.66	1.33	4.73	4.73	4.17 ± 2.89	-2.93	1.27	1.80	
0.1	6.29	LTE	5.09	1.39	2.28 ± 2.23	-66.88	4.40	2.10	2.10	2.19 ± 2.65	-35.58	1.16	1.04	
		NLTE	5.71	1.59	2.56 ± 2.45	-75.75	4.47	2.15	2.15	2.27 ± 2.69	-36.60	1.28	1.13	
5	5.59	LTE	3.93	1.01	1.56 ± 1.75	-45.52	2.91	1.15	1.15	1.19 ± 1.88	-19.63	1.35	1.32	
		NLTE	4.03	1.05	1.65 ± 1.81	-47.67	2.96	1.19	1.19	1.16 ± 1.89	-19.10	1.36	1.42	
10	4.01	LTE	3.42	6.65	9.98 ± 1.23	-36.26	2.17	5.66	5.66	5.66 ± 1.24	-11.71	1.57	1.76	
		NLTE	3.47	6.84	1.03 ± 1.26	-36.97	2.25	5.97	5.97	5.47 ± 1.23	-11.43	1.54	1.88	
20	1.83	LTE	1.88	1.44	1.84 ± 4.43	-11.26	1.40	0.99	0.99	0.57 ± 0.49	-2.36	1.35	3.20	
		NLTE	1.95	1.54	2.32 ± 0.47	-14.40	1.37	0.92	0.92	0.41 ± 0.49	-1.68	1.42	5.66	

Table A2 continued

Table A2 (continued)

Model	day	L_{bol} ($\times 10^{42}$)	H-Opacity	$A(\text{H}\alpha)_{\text{CN}}$	$A(\text{H}\alpha)_{\text{CS}}$ ($\times 10^{-2}$)	$F(\text{H}\alpha)$ ($\times 10^{-1}$)	EW($\text{H}\alpha$)	$A(\text{H}\beta)_{\text{CN}}$	$A(\text{H}\alpha)_{\text{CS}}$ ($\times 10^{-2}$)	$F(\text{H}\beta)$ ($\times 10^{-1}$)	EW($\text{H}\beta$)	$A(\text{H}\alpha)_{\text{CN}}/$ $A(\text{H}\alpha)_{\text{CS}}$	$F(\text{H}\alpha)/$ $F(\text{H}\beta)$
(1)	(2)	(3)	(4)	(5)	(6)	(7)	(8)	(9)	(10)	(11)	(12)	(13)	(14)
B7	0.1	8.98	LTE	7.19	2.55	4.39 \pm 3.77	-106.57	4.35	2.87	2.92 \pm 3.63	-34.14	1.65	1.50
			NLTE	7.55	2.76	4.66 \pm 4.01	-110.65	4.47	2.96	2.91 \pm 3.68	-34.01	1.69	1.60
	5	8.14	LTE	5.20	1.80	3.13 \pm 2.92	-72.91	3.32	1.95	1.74 \pm 2.80	-20.67	1.56	1.80
			NLTE	5.59	2.00	3.34 \pm 3.12	-76.82	3.39	2.04	1.82 \pm 2.88	-21.37	1.65	1.84
	10	6.44	LTE	4.33	1.25	2.06 \pm 2.13	-54.61	2.70	1.22	1.18 \pm 2.09	-16.47	1.60	1.75
			NLTE	4.77	1.43	2.36 \pm 2.35	-62.26	2.70	1.24	1.18 \pm 2.12	-16.20	1.77	2.00
B8	20	3.62	LTE	2.56	4.22	6.14 \pm 9.49	-22.68	1.59	2.80	2.53 \pm 1.03	-5.31	1.61	2.42
			NLTE	2.67	4.50	6.74 \pm 9.88	-25.01	1.60	2.86	2.47 \pm 1.04	-5.14	1.68	2.72
	0.1	5.11	LTE	2.83	0.06	0.89 \pm 0.13	-26.40	1.59	0.30	2.69 \pm 1.10	-5.27	1.79	3.31
			NLTE	2.64	5.45	7.44 \pm 1.17	-22.33	1.52	2.65	2.81 \pm 1.09	-5.53	1.73	2.65
	5	3.61	LTE	2.20	3.20	4.78 \pm 8.37	-17.87	1.68	2.80	3.29 \pm 9.32	-8.02	1.31	1.45
			NLTE	2.28	3.39	4.93 \pm 0.85	-18.54	1.70	2.89	3.31 \pm 0.94	-8.01	1.34	1.49
B9	10	2.68	LTE	1.63	1.33	1.92 \pm 0.53	-9.18	1.73	2.35	2.21 \pm 0.72	-6.85	0.95	0.87
			NLTE	1.77	1.60	2.28 \pm 0.55	-10.95	1.69	2.23	1.86 \pm 7.11	-5.73	1.05	1.22
	20	1.55	LTE	1.48	0.62	0.98 \pm 0.31	-7.57	1.32	0.66	0.51 \pm 0.41	-2.51	1.11	1.93
			NLTE	1.48	0.63	0.91 \pm 0.31	-6.96	1.38	0.76	0.25 \pm 0.40	-1.23	1.08	3.67
	0.1	8.82	LTE	4.12	15.50	24.50 \pm 26.60	-49.29	2.80	15.20	15.90 \pm 25.30	-18.80	1.47	1.54
			NLTE	4.23	16.10	24.80 \pm 27.10	-49.72	2.78	14.90	14.00 \pm 24.50	-16.67	1.52	1.77
B9	5	7.03	LTE	2.52	7.18	11.50 \pm 16.70	-24.34	2.61	12.20	11.10 \pm 21.20	-14.62	0.97	1.03
			NLTE	2.76	8.33	12.70 \pm 17.80	-26.79	2.60	12.00	10.80 \pm 20.90	-14.29	1.06	1.18
	10	5.15	LTE	1.84	3.26	4.46 \pm 1.05	-26.79	2.27	7.82	6.46 \pm 1.56	-14.29	0.81	0.69
			NLTE	2.00	3.87	5.23 \pm 1.10	-11.50	2.22	7.47	6.37 \pm 1.54	-10.50	0.90	0.82
	20	2.87	LTE	1.72	1.79	1.64 \pm 6.11	-13.55	1.45	1.69	1.45 \pm 7.73	-10.36	1.18	1.13
			NLTE	1.76	1.87	1.96 \pm 6.22	-6.55	1.48	1.77	1.22 \pm 7.60	-3.89	1.19	1.61

Table A2 continued

Table A2 (continued)

Model	day	L_{bol} ($\times 10^{42}$)	H-Opacity	$A(\text{H}\alpha)_{\text{CN}}$	$A(\text{H}\alpha)_{\text{CS}}$ ($\times 10^{-2}$)	$F(\text{H}\alpha)$ ($\times 10^{-1}$)	EW($\text{H}\alpha$)	$A(\text{H}\beta)_{\text{CN}}$	$A(\text{H}\alpha)_{\text{CS}}$ ($\times 10^{-2}$)	$F(\text{H}\beta)$ ($\times 10^{-1}$)	EW($\text{H}\beta$)	$A(\text{H}\alpha)_{\text{CN}}/$ $A(\text{H}\alpha)_{\text{CS}}$	$F(\text{H}\alpha)/$ $F(\text{H}\beta)$
(1)	(2)	(3)	(4)	(5)	(6)	(7)	(8)	(9)	(10)	(11)	(12)	(13)	(14)
B10	0.1	13.10	LTE	5.41	2.74	4.60±4.34	-73.82	4.67	4.27	4.38±5.18	-37.53	1.16	1.05
			NLTE	5.52	2.84	4.96±4.54	-78.99	4.68	4.27	4.04±5.09	-34.77	1.18	1.23
	5	17.00	LTE	3.54	1.55	2.71±2.95	-44.40	3.69	2.95	3.03±4.04	-27.60	0.96	0.90
			NLTE	3.60	1.60	2.72±2.99	-44.37	3.58	2.83	2.92±3.94	-26.60	1.00	0.93
	10	8.26	LTE	2.39	0.75	1.19±0.18	-22.06	2.70	1.59	1.58±0.27	-16.90	0.89	0.75
			NLTE	2.62	0.88	1.39±0.20	-25.52	2.75	1.62	1.56±0.27	-16.82	0.95	0.89
B11	20	4.76	LTE	2.14	0.45	5.33±1.15	-13.58	1.62	0.38	2.41±1.31	-3.88	1.32	2.21
			NLTE	2.24	4.84	6.28±1.20	-16.11	1.63	3.88	2.63±1.30	-4.27	1.38	2.39
	0.1	18.10	LTE	3.44	1.41	3.71 ± 3.62	-53.12	5.50	6.77	7.30 ± 7.89	-48.46	0.63	0.51
			NLTE	7.40	4.47	8.09 ± 6.70	-115.40	5.48	6.71	6.87 ± 7.75	-45.81	1.35	1.18
	5	15.70	LTE	2.49	0.91	2.33±0.29	-31.79	4.05	4.48	4.80±5.96	-32.58	0.62	0.48
			NLTE	4.76	2.81	5.13±4.78	-68.45	4.11	4.57	4.76±5.97	-32.39	1.16	1.08
B12	10	12.90	LTE	3.13	1.50	2.78±3.13	-39.34	2.85	2.47	2.65±4.14	-19.79	1.10	1.05
			NLTE	3.45	1.74	3.00±3.34	-42.32	2.82	2.48	2.65±4.19	-19.49	1.22	1.13
	20	8.29	LTE	2.53	8.86	1.29 ± 2.01	-22.12	1.86	8.85	5.89 ± 2.31	-5.73	1.36	2.18
			NLTE	2.86	1.08	1.63±2.25	-28.07	1.93	9.60	6.82±2.37	-6.60	1.48	2.39
	0.1	10.80	LTE	1.44	2.97	3.89±1.57	-5.71	1.21	2.21	2.81±2.14	-2.61	1.19	1.38
			NLTE	1.45	3.05	4.54±1.60	-6.69	1.07	8.05	5.13±2.03	-0.48	1.35	8.85
B12	5	7.13	LTE	1.63	3.26	4.76±1.31	-9.16	1.21	1.65	2.31±1.59	-2.91	1.35	2.06
			NLTE	1.52	2.72	3.57±1.25	-6.79	1.18	1.46	1.76±1.56	-2.23	1.28	2.03
	10	4.73	LTE	1.77	2.86	4.41±1.00	-11.89	1.25	1.39	1.50±1.09	-2.74	1.41	2.94
			NLTE	1.72	2.68	3.93±0.98	-10.57	1.26	1.45	1.89±1.11	-3.43	1.36	2.08
	20	3.26	LTE	1.32	0.87	0.09±0.06	-3.47	1.30	1.19	0.10±0.08	-2.42	1.01	1.00
			NLTE	1.45	1.24	0.20±0.07	-7.09	1.26	1.00	0.09±0.08	-2.38	1.16	2.09

Table A2 continued

Table A2 (continued)

Model	day	L_{bol} ($\times 10^{42}$)	H-Opacity	$A(\text{H}\alpha)_{\text{CN}}$	$A(\text{H}\alpha)_{\text{CS}}$ ($\times 10^{-2}$)	$F(\text{H}\alpha)$ ($\times 10^{-1}$)	EW($\text{H}\alpha$)	$A(\text{H}\beta)_{\text{CN}}$	$A(\text{H}\alpha)_{\text{CS}}$ ($\times 10^{-2}$)	$F(\text{H}\beta)$ ($\times 10^{-1}$)	EW($\text{H}\beta$)	$A(\text{H}\alpha)_{\text{CN}}/$ $A(\text{H}\alpha)_{\text{CS}}$	$F(\text{H}\alpha)/$ $F(\text{H}\beta)$
(1)	(2)	(3)	(4)	(5)	(6)	(7)	(8)	(9)	(10)	(11)	(12)	(13)	(14)
B13	0.1	18.40	LTE	1.99	9.56	0.15 \pm 0.03	-15.12	1.44	7.48	0.70 \pm 0.36	-4.06	1.38	2.11
			NLTE	1.95	9.24	0.15 \pm 0.03	-13.27	1.43	7.32	0.82 \pm 0.36	-4.77	1.37	1.58
	5	13.60	LTE	2.11	9.67	0.15 \pm 0.03	-17.25	1.57	8.35	0.76 \pm 0.31	-5.25	1.34	1.97
			NLTE	1.92	8.05	0.15 \pm 0.03	-14.49	1.45	6.56	0.66 \pm 0.30	-4.54	1.33	1.92
	10	8.84	LTE	2.01	6.46	1.05 \pm 0.19	-16.51	1.79	8.27	0.63 \pm 0.23	-6.06	1.12	1.79
			NLTE	2.12	7.17	1.12 \pm 0.20	-17.44	1.82	8.50	0.80 \pm 0.24	-7.73	1.16	1.82
B14	20	5.57	LTE	1.32	1.47	1.45 \pm 1.00	-3.12	1.60	4.25	0.45 \pm 0.35	-4.56	0.82	0.35
			NLTE	1.46	2.16	2.63 \pm 1.08	-5.62	1.52	3.69	0.92 \pm 0.59	-4.04	0.96	0.59
	0.1	28.40	LTE	2.86	21.7	38.3 \pm 47.2	-32.86	2.20	27.4	26.8 \pm 58.1	-11.73	1.30	1.43
			NLTE	2.76	20.7	33.4 \pm 44.9	-28.40	2.13	25.9	26.8 \pm 57.7	-11.72	1.30	1.24
	5	22.7	LTE	2.78	20.7	36.3 \pm 46.0	-31.14	2.09	23.8	25.8 \pm 54.8	-11.84	1.33	1.41
			NLTE	2.55	18.3	32.7 \pm 43.7	-27.74	1.93	20.2	19.3 \pm 51.5	-8.88	1.32	1.69
B15	10	15.40	LTE	2.80	16.9	29.5 \pm 37.2	-31.46	2.51	25.4	26.4 \pm 46.9	-15.73	1.12	1.12
			NLTE	2.84	17.3	28.8 \pm 37.2	-30.57	2.36	22.9	23.4 \pm 45.0	-13.90	1.20	1.23
	20	8.83	LTE	1.68	4.59	5.58 \pm 1.70	-8.22	1.80	8.94	7.79 \pm 2.53	-6.94	0.93	0.72
			NLTE	1.74	5.08	7.66 \pm 1.82	-11.21	1.74	8.34	7.75 \pm 2.52	-6.89	1.00	0.99
	0.1	41.00	LTE	4.44	4.32	7.97 \pm 7.58	-63.24	3.42	6.67	6.97 \pm 9.60	-25.29	1.30	1.14
			NLTE	4.26	4.11	8.09 \pm 7.55	-63.83	3.23	6.16	6.05 \pm 9.10	-21.93	1.32	1.34
B15	5	35.40	LTE	3.96	4.00	7.39 \pm 7.37	-54.59	3.16	6.16	6.45 \pm 9.39	-22.62	1.25	1.15
			NLTE	3.96	4.01	7.58 \pm 7.45	-55.77	3.10	6.02	6.25 \pm 9.28	-21.82	1.28	1.21
	10	26.60	LTE	4.07	3.78	7.17 \pm 6.95	-58.17	3.39	5.97	6.74 \pm 8.84	-26.94	1.20	1.06
			NLTE	4.20	3.97	7.37 \pm 7.15	-59.37	3.26	5.69	6.00 \pm 8.52	-23.83	1.29	1.23
	20	15.10	LTE	1.72	6.88	1.13 \pm 2.56	-11.83	2.32	2.32	2.52 \pm 4.74	-14.28	0.74	0.45
			NLTE	2.58	1.52	2.57 \pm 3.53	-26.69	2.33	2.33	2.56 \pm 4.75	-14.54	1.11	1.00

NOTE—The amplitudes have suffices CN and CS for continuum normalized and continuum subtracted spectrum, respectively. The continuum subtracted spectrum has a unit of $\text{erg cm}^{-2} \text{s}^{-1} \text{Å}^{-1}$. The line integrated flux in the units of $\text{erg cm}^{-2} \text{s}^{-1}$ is estimated using the line_flux routine from the Spectutils Python package.

REFERENCES

- Asplund, M., Grevesse, N., Sauval, A. J., & Scott, P. 2009, *ARA&A*, 47, 481, doi: [10.1146/annurev.astro.46.060407.145222](https://doi.org/10.1146/annurev.astro.46.060407.145222)
- Astropy Collaboration, Price-Whelan, A. M., Lim, P. L., et al. 2022, *ApJ*, 935, 167, doi: [10.3847/1538-4357/ac7c74](https://doi.org/10.3847/1538-4357/ac7c74)
- Baer, M. J. 2024, Duperfit, v0.1.0, Zenodo, doi: [10.5281/zenodo.10992738](https://doi.org/10.5281/zenodo.10992738)
- Bellm, E. C., Kulkarni, S. R., Graham, M. J., et al. 2019, *PASP*, 131, 018002, doi: [10.1088/1538-3873/aaeabe](https://doi.org/10.1088/1538-3873/aaeabe)
- Benetti, S., Nicholl, M., Cappellaro, E., et al. 2014, *MNRAS*, 441, 289, doi: [10.1093/mnras/stu538](https://doi.org/10.1093/mnras/stu538)
- Blinnikov, S., & Sorokina, E. 2004, *Ap&SS*, 290, 13, doi: [10.1023/B:ASTR.0000022161.03559.42](https://doi.org/10.1023/B:ASTR.0000022161.03559.42)
- Blinnikov, S. I., & Bartunov, O. S. 1993, *A&A*, 273, 106
- Blinnikov, S. I., Eastman, R., Bartunov, O. S., Popolitov, V. A., & Woosley, S. E. 1998, *ApJ*, 496, 454, doi: [10.1086/305375](https://doi.org/10.1086/305375)
- Blinnikov, S. I., Röpke, F. K., Sorokina, E. I., et al. 2006, *A&A*, 453, 229, doi: [10.1051/0004-6361:20054594](https://doi.org/10.1051/0004-6361:20054594)
- Cardelli, J. A., Clayton, G. C., & Mathis, J. S. 1989, *ApJ*, 345, 245, doi: [10.1086/167900](https://doi.org/10.1086/167900)
- Chatzopoulos, E., Wheeler, J. C., & Vinko, J. 2012, *ApJ*, 746, 121, doi: [10.1088/0004-637X/746/2/121](https://doi.org/10.1088/0004-637X/746/2/121)
- Chatzopoulos, E., Wheeler, J. C., Vinko, J., et al. 2011, *ApJ*, 729, 143, doi: [10.1088/0004-637X/729/2/143](https://doi.org/10.1088/0004-637X/729/2/143)
- Chevalier, R. A., & Fransson, C. 1994, *ApJ*, 420, 268, doi: [10.1086/173557](https://doi.org/10.1086/173557)
- Chevalier, R. A., & Irwin, C. M. 2011, *ApJL*, 729, L6, doi: [10.1088/2041-8205/729/1/L6](https://doi.org/10.1088/2041-8205/729/1/L6)
- Cooke, J., Sullivan, M., Gal-Yam, A., et al. 2012, *Nature*, 491, 228, doi: [10.1038/nature11521](https://doi.org/10.1038/nature11521)
- Cover, T. M., & Hart, P. E. 1967, *IEEE Transactions on Information Theory*, 13, 21, doi: [10.1109/TIT.1967.1053964](https://doi.org/10.1109/TIT.1967.1053964)
- Dessart, L., Audit, E., & Hillier, D. J. 2015, *MNRAS*, 449, 4304, doi: [10.1093/mnras/stv609](https://doi.org/10.1093/mnras/stv609)
- Dessart, L., & Hillier, D. J. 2010, *MNRAS*, 405, 2141, doi: [10.1111/j.1365-2966.2010.16611.x](https://doi.org/10.1111/j.1365-2966.2010.16611.x)
- Dessart, L., Hillier, D. J., Audit, E., Livne, E., & Waldman, R. 2016, *MNRAS*, 458, 2094, doi: [10.1093/mnras/stw336](https://doi.org/10.1093/mnras/stw336)
- Dessart, L., Hillier, D. J., & Kunzarayakti, H. 2022, *A&A*, 658, A130, doi: [10.1051/0004-6361/202142436](https://doi.org/10.1051/0004-6361/202142436)
- Dessart, L., Hillier, D. J., Woosley, S. E., & Kunzarayakti, H. 2023, *A&A*, 677, A7, doi: [10.1051/0004-6361/202346626](https://doi.org/10.1051/0004-6361/202346626)
- Dessart, L., & Jacobson-Galán, W. V. 2023, *A&A*, 677, A105, doi: [10.1051/0004-6361/202346754](https://doi.org/10.1051/0004-6361/202346754)
- Dessart, L., Ryu, T., Amaro Seoane, P., & Taylor, A. M. 2024, *A&A*, 682, A58, doi: [10.1051/0004-6361/202348228](https://doi.org/10.1051/0004-6361/202348228)
- Drake, A. J., Djorgovski, S. G., Prieto, J. L., et al. 2010, *ApJL*, 718, L127, doi: [10.1088/2041-8205/718/2/L127](https://doi.org/10.1088/2041-8205/718/2/L127)
- Duncan, R. C., & Thompson, C. 1992, *ApJL*, 392, L9, doi: [10.1086/186413](https://doi.org/10.1086/186413)
- Earl, N., Tollerud, E., O'Steen, R., et al. 2022, *astropy/specutils*: V1.8.0, Zenodo, doi: [10.5281/ZENODO.7015214](https://doi.org/10.5281/ZENODO.7015214)
- Gal-Yam, A. 2012, *Science*, 337, 927, doi: [10.1126/science.1203601](https://doi.org/10.1126/science.1203601)
- Ginzburg, S., & Balberg, S. 2012, *ApJ*, 757, 178, doi: [10.1088/0004-637X/757/2/178](https://doi.org/10.1088/0004-637X/757/2/178)
- Glebbeek, E., Gaburov, E., de Mink, S. E., Pols, O. R., & Portegies Zwart, S. F. 2009, *A&A*, 497, 255, doi: [10.1051/0004-6361/200810425](https://doi.org/10.1051/0004-6361/200810425)
- Gomez, S., Berger, E., Blanchard, P. K., et al. 2020, *ApJ*, 904, 74, doi: [10.3847/1538-4357/abbf49](https://doi.org/10.3847/1538-4357/abbf49)
- Harris, C. R., Millman, K. J., van der Walt, S. J., et al. 2020, *Nature*, 585, 357, doi: [10.1038/s41586-020-2649-2](https://doi.org/10.1038/s41586-020-2649-2)
- Howell, D. A., Sullivan, M., Perrett, K., et al. 2005, *ApJ*, 634, 1190, doi: [10.1086/497119](https://doi.org/10.1086/497119)
- Inserra, C., Smartt, S. J., Jerkstrand, A., et al. 2013, *ApJ*, 770, 128, doi: [10.1088/0004-637X/770/2/128](https://doi.org/10.1088/0004-637X/770/2/128)
- Ivezic, Z., Axelrod, T., Brandt, W. N., et al. 2008, *Serbian Astronomical Journal*, 176, 1, doi: [10.2298/SAJ0876001I](https://doi.org/10.2298/SAJ0876001I)
- Kaiser, N., Aussel, H., Burke, B. E., et al. 2002, in *Society of Photo-Optical Instrumentation Engineers (SPIE) Conference Series*, Vol. 4836, Survey and Other Telescope Technologies and Discoveries, ed. J. A. Tyson & S. Wolff, 154–164, doi: [10.1117/12.457365](https://doi.org/10.1117/12.457365)
- Kasen, D., & Bildsten, L. 2010, *ApJ*, 717, 245, doi: [10.1088/0004-637X/717/1/245](https://doi.org/10.1088/0004-637X/717/1/245)
- McKinney, W., et al. 2010, in *Proceedings of the 9th Python in Science Conference*, Vol. 445, Austin, TX, 51–56
- Metzger, B. D., Vurm, I., Hascoët, R., & Beloborodov, A. M. 2014, *MNRAS*, 437, 703, doi: [10.1093/mnras/stt1922](https://doi.org/10.1093/mnras/stt1922)
- Neter, J., Kutner, M. H., Nachtsheim, C. J., Wasserman, W., et al. 1996, *Applied linear statistical models*, 4th edn. (McGraw-Hill Irwin Chicago)
- Nicholl, M. 2021, *Astronomy and Geophysics*, 62, 5.34, doi: [10.1093/astrogeo/atab092](https://doi.org/10.1093/astrogeo/atab092)
- Nicholl, M., Berger, E., Smartt, S. J., et al. 2016a, *ApJ*, 826, 39, doi: [10.3847/0004-637X/826/1/39](https://doi.org/10.3847/0004-637X/826/1/39)
- Nicholl, M., Berger, E., Margutti, R., et al. 2016b, *ApJL*, 828, L18, doi: [10.3847/2041-8205/828/2/L18](https://doi.org/10.3847/2041-8205/828/2/L18)
- Nugis, T., & Lamers, H. J. G. L. M. 2000, *A&A*, 360, 227
- Ofek, E. O., Cameron, P. B., Kasliwal, M. M., et al. 2007, *ApJL*, 659, L13, doi: [10.1086/516749](https://doi.org/10.1086/516749)

- Paxton, B., Bildsten, L., Dotter, A., et al. 2011, *ApJS*, 192, 3, doi: [10.1088/0067-0049/192/1/3](https://doi.org/10.1088/0067-0049/192/1/3)
- Paxton, B., Cantiello, M., Arras, P., et al. 2013, *ApJS*, 208, 4, doi: [10.1088/0067-0049/208/1/4](https://doi.org/10.1088/0067-0049/208/1/4)
- Paxton, B., Marchant, P., Schwab, J., et al. 2015, *ApJS*, 220, 15, doi: [10.1088/0067-0049/220/1/15](https://doi.org/10.1088/0067-0049/220/1/15)
- Paxton, B., Schwab, J., Bauer, E. B., et al. 2018, *ApJS*, 234, 34, doi: [10.3847/1538-4365/aaa5a8](https://doi.org/10.3847/1538-4365/aaa5a8)
- Paxton, B., Smolec, R., Schwab, J., et al. 2019, *ApJS*, 243, 10, doi: [10.3847/1538-4365/ab2241](https://doi.org/10.3847/1538-4365/ab2241)
- Pedregosa, F., Varoquaux, G., Gramfort, A., et al. 2011, *Journal of Machine Learning Research*, 12, 2825
- Price-Whelan, A. M., Sipőcz, B., Günther, H., et al. 2018, *The Astronomical Journal*, 156, 123
- Quimby, R. M., Yuan, F., Akerlof, C., & Wheeler, J. C. 2013, *MNRAS*, 431, 912, doi: [10.1093/mnras/stt213](https://doi.org/10.1093/mnras/stt213)
- Quimby, R. M., Kulkarni, S. R., Kasliwal, M. M., et al. 2011, *Nature*, 474, 487, doi: [10.1038/nature10095](https://doi.org/10.1038/nature10095)
- Quimby, R. M., De Cia, A., Gal-Yam, A., et al. 2018, *ApJ*, 855, 2, doi: [10.3847/1538-4357/aaac2f](https://doi.org/10.3847/1538-4357/aaac2f)
- Schlegel, E. M. 1990, *MNRAS*, 244, 269
- Shappee, B. J., Prieto, J. L., Grupe, D., et al. 2014, *ApJ*, 788, 48, doi: [10.1088/0004-637X/788/1/48](https://doi.org/10.1088/0004-637X/788/1/48)
- Smith, M., Sullivan, M., Nichol, R. C., et al. 2018, *ApJ*, 854, 37, doi: [10.3847/1538-4357/aaa126](https://doi.org/10.3847/1538-4357/aaa126)
- Smith, N., Chornock, R., Li, W., et al. 2008, *ApJ*, 686, 467, doi: [10.1086/591021](https://doi.org/10.1086/591021)
- Smith, N., & McCray, R. 2007, *ApJL*, 671, L17, doi: [10.1086/524681](https://doi.org/10.1086/524681)
- Smith, N., Li, W., Foley, R. J., et al. 2007, *ApJ*, 666, 1116, doi: [10.1086/519949](https://doi.org/10.1086/519949)
- Vink, J. S., de Koter, A., & Lamers, H. J. G. L. M. 2001, *A&A*, 369, 574, doi: [10.1051/0004-6361:20010127](https://doi.org/10.1051/0004-6361:20010127)
- Wagle, G. 2023, *SuperLite: IMC-DDMC Radiation Transport Code for Interacting Transients*, r1.0.0, Zenodo, doi: [10.5281/zenodo.8111119](https://doi.org/10.5281/zenodo.8111119)
- Wagle, G. A., Chatzopoulos, E., Wollaeger, R. T., & Fontes, C. J. 2023, *ApJ*, 953, 132, doi: [10.3847/1538-4357/acda23](https://doi.org/10.3847/1538-4357/acda23)
- Wollaeger, R. T., & van Rossum, D. R. 2014, *ApJS*, 214, 28, doi: [10.1088/0067-0049/214/2/28](https://doi.org/10.1088/0067-0049/214/2/28)
- Wollaeger, R. T., van Rossum, D. R., Graziani, C., et al. 2013, *ApJS*, 209, 36, doi: [10.1088/0067-0049/209/2/36](https://doi.org/10.1088/0067-0049/209/2/36)
- Woosley, S. E. 2010, *ApJL*, 719, L204, doi: [10.1088/2041-8205/719/2/L204](https://doi.org/10.1088/2041-8205/719/2/L204)